Master's Thesis

Monte Carlo event generation and model validation for lepton universality

Monte-Carlo-Ereignisgenerierung und Modellvalidierung für Lepton-Universalität

prepared by

Uday Saidev Polisetty

from Lakkavaram, India

at the II. Institute of Physics

Abstract

The Standard Model predicts that the probability of electroweak decay of W or Z bosons to different flavour leptons should be the same. This is given by lepton universality, which gives the ratio of the decay of W or Z bosons to different flavours of leptons as unity. Previous ATLAS measurements showed a consistent result in support of lepton universality. A recent measurement by LHCb hinted at a violation of lepton flavour universality, with a significance of 3.1 standard deviations. In this analysis, Physics Beyond the Standard Model (BSM) is studied to explain this potential violation.

This analysis probes the lepton universality by studying the BSM models such as a Charged Higgs boson, Leptoquarks, or the possible evidence of a W' boson in the single lepton final state of the top-antitop pair production at the centre-of-mass energy of 13 TeV with the ATLAS experiment. The events generated are folded to reco-level and statistical fit only limits are obtained on the BSM models.

Contents

Contents

1. Introduction

The key to understanding the laws of nature lies in particle physics. It is the study of the elementary particles that comprise the fundamental constituents of the universe and their interactions. Over the last century, particles were discovered and theories were developed and brought to the current understanding embodied in the Standard Model (SM) of particle physics which combines the theory of electromagnetic and weak interaction, developed by Glashow, Weinberg, and Salam [1–3], with quantum chromodynamics (QCD), the theory of strong interaction between quarks and gluons [4][5]. The SM is renormalisable and therefore predicts cross-sections that are finite [6][7]. It is one of the most successful theories in modern physics. So far, several experiments at the Large Hadron Collider (LHC), the Tevatron, Large Electron-Positron Collider (LEP), HERA, etc, have performed rigid tests of the SM. The crowning achievement is the discovery of the Higgs boson in 2012 by the ATLAS [8] and CMS [9] experiments.

Nonetheless, the theory still has its limitations [10]. Neutrinos are massless in the SM but it is proven otherwise with the observed neutrino flavour oscillations [11]. Gravitational force is not described in the Standard Model, and nor is Dark matter [12]. There is a need to develop the SM to a new theory in order to describe the unanswered questions by the SM. One such question is tackled in my master thesis. The SM predicts Lepton universality. The coupling of gauge bosons to leptons is universal ignoring the minor mass effects. Measurements at the LHCb [13], BELLE [14] experiments hint at possible violation of lepton universality which implies effects Beyond the Standard Model (BSM). My thesis focuses on studying and analysing the simplified models in BSM that could explain the possible violation.

2. Theoretical background

This section provides a brief theoretical introduction to the Standard Model of particle physics. An introduction to physics Beyond the Standard Model is given in Section 2.4. and the software description used in the analysis is given in Chapter 4.

2.1. The fundamental particles of the Standard Model and their interactions

The SM contains two classes of particles, fermions with half-integer spin (spin 1/2) and gauge bosons with integer spin (spin 1). In addition, there is a scalar particle (spin 0), the Higgs boson. In total, The SM comprises a set of 17 fundamental particles (12 fermions and 5 bosons). A graphical representation is provided in figure 2.1.

The 12 fermions are divided again into two groups, leptons, and quarks, each group with three generations. Three generations of leptons contain a lepton and its associated neutrino. They form a weak isospin doublet. The first generation is made of the electron with an electric charge -1e and the electron neutrino with no charge. The second generation is the muon (charge -1e) and the muon neutrino. The third generation is the tau (charge -1e) and the tau neutrino. Neutrinos are chargeless particles. Their behaviour is quite different. They have a tiny mass and are stable but oscillate between the three generations [11].

Quarks are also found in three generations, each generation contains an up-type quark and a down-type quark. Up-type quarks have a charge of $+2/3e$ and a down-type quark has a charge of -1/3e. The first generation is up and down quark, the second generation is charm and strange quark, and the third generation is the top and bottom quark. As the generation goes up, the mass of the fermions increases. Ordinary matter is made of protons, neutrons, and electrons. Protons and neutrons are hadrons with first generation quark content. Higher generations will decay to stable first generation particles. Quarks do not propagate freely and are observed as jets of colourless particles. The process by
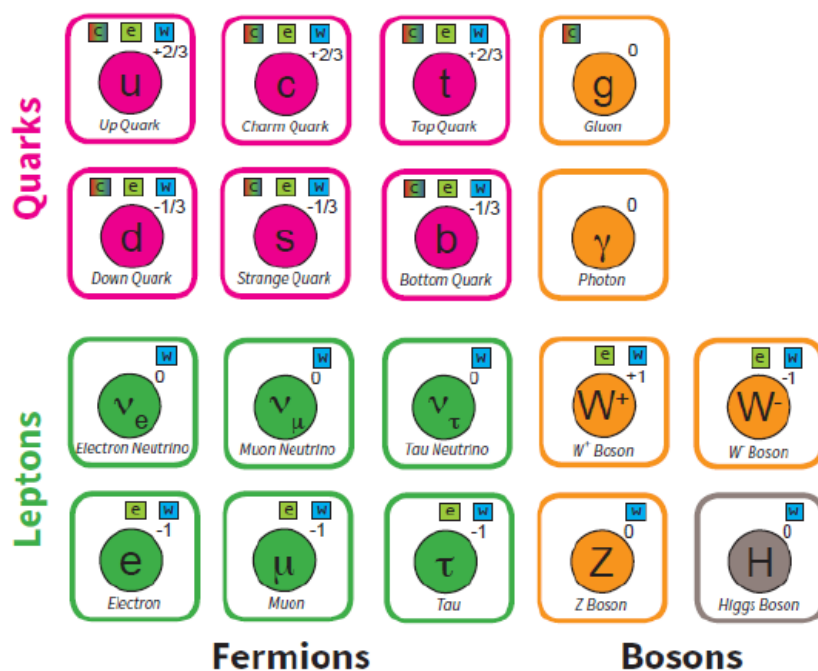
Figure 2.1.: A graphical representation of Standard Model particles. The electric charge of particles is shown in the upper right corner and the particle's couplings are represented as c=colour, e=electromagnetic, and w=weak. Courtesy of Boris Lemmer.

which high-energy quarks (and gluons) produce jets is known as hadronisation.

Free fermions are described by spinor fields Ψ which obey the Dirac equation (equation 2.1) [15]. The negative solutions can be interpreted as anti-particles. All 12 fermions have their own antiparticle with opposite charge. In the SM neutrinos are massless and have no charge. They are similar to the anti-neutrinos. This opens up the possibility that neutrinos are their own antiparticles (also called Majorana fermions) but in contradiction with the observation of neutrino flavour oscillations, it is yet unclear if by addition of a mass term for neutrinos, whether it would be a Dirac or Majorana mass term, or both.

2.1. The fundamental particles of the Standard Model and their interactions

The Dirac equation [15] is given by

$$(i\gamma^\mu \partial_\mu - m)\psi = 0 \ , \tag{2.1}$$

where ψ is the particle spinor, m is the mass of the particle, and γ^μ is given by the Dirac matrices.

There are four fundamental forces: gravitational, electromagnetic, weak, and strong force. The gravitational force is not described in the SM. General relativity is the theory of the gravitational force. The rest is described by the local gauge principle where each interaction is described by a different symmetry group. In the following, these groups are described:

Fermions interact with each other through the exchange of elementary particles called gauge bosons. They are the force carriers for fermions. For the electromagnetic force, fermions interact via the photon. Photons couple only to charged particles. Neutrinos do not couple to photons. The electromagnetic interaction is described by the U(1) symmetry. The Dirac equation (see equation 2.1) is modified to add the interaction via photon mediator. It is gauge invariant under local U(1) transformation. The equation is given by:

$$i\gamma^\mu (\partial_\mu + iqA_\mu)\psi - m\psi = 0 \ , \tag{2.2}$$

where q is the charge of the particle, A_μ the gauge field, (in this case, the photon field) and $q\gamma^\mu A_\mu \psi$ is the interaction term.

The weak force is described in the SU(2) symmetry (special unitary (2) group). It couples to a particle property, the third component of weak isospin (T_3). The Lagrangian of the weak force is invariant under SU(2) transformation, this brings the requirement of three massive gauge bosons. Two of them are the charged W bosons (W^+ and W^-). The third is a neutral weak gauge boson (Z boson). The mass of the Z^0 boson is 91.2 GeV and the mass of the W boson is 80.4 GeV [16]. The masses of the gauge bosons are explained by the Higgs mechanism (see Section 2.2). Left-handed particles form isospin doublets. The two fermions in each generation form an isospin doublet. Left-handed particles are grouped in doublets with weak isospin of $\frac{1}{2}$. W boson is parity violating [17, 18] as they can only interact with the left-handed particles and right-handed anti-particles. This coupling is called V-A coupling (vector-axial vector coupling).

2. Theoretical background

Similarly, the neutral weak gauge boson should couple to left-handed particles and right-handed anti-particles alone but the neutral boson also couples to right-handed charged leptons. This behaviour is explained by the GWS mechanism (Glashow-Weinberg-Salam mechanism)[2, 3]. It introduces the $U(1)_Y$ symmetry. The gauge field couples to hypercharge Y. This behaviour is explained via the unification of electromagnetic force and weak force.

The electroweak force results from the $SU(2)_L \times U(1)_Y$ gauge symmetry. Hypercharge (Y) relates electric charge (Q) and the third component of weak isospin (T_3) via:

$$Y = 2(Q - T_3) \tag{2.3}$$

This gauge field and the neutral gauge field of the weak force mix to form the photon field and the Z field:

$$\begin{pmatrix} A_\mu \\ Z_\mu \end{pmatrix} = \begin{pmatrix} \cos(\theta_W) & \sin(\theta_W) \\ -\sin(\theta_W) & \cos(\theta_W) \end{pmatrix} \begin{pmatrix} B_\mu \\ W_\mu^{(3)} \end{pmatrix} \tag{2.4}$$

The photon and the Z boson are the resulting mediators. Electroweak mixing angle or Weinberg angle (θ_W) gives the mixing.

The strong force is described by the $SU(3)$ symmetry and the property associated with it is the colour charge. There are only three colours, blue, green, and red. In the strong force, the interactions are mediated by the exchange of colourless particles called gluons. There are no quarks without colour.

The mixing between the three quark families is given by the Cabibbo-Kobayashi-Maskawa (CKM) matrix [19][20]. It is a 3×3 unitary matrix in which information on the strength of the flavour changing weak interactions is given. Mass eigen-states are not equal to the weak eigen-states. CKM matrix relates the mass eigenstates of the down-type

quarks to their corresponding weak eigenstates[1]. CKM matrix is shown in equation 2.5.

$$\begin{pmatrix} d' \\ s' \\ b' \end{pmatrix} = \begin{pmatrix} V_{ud} & V_{us} & V_{ub} \\ V_{cd} & V_{cs} & V_{cb} \\ V_{td} & V_{ts} & V_{tb} \end{pmatrix} \begin{pmatrix} d \\ s \\ b \end{pmatrix} \tag{2.5}$$

2.2. The Higgs mechanism

Mathematically, the SM can be described by three gauge groups $SU(3)_C \times SU(2)_L \times U(1)_Y$, where each group stands for one interaction. $SU(3)_C$ for QCD, $SU(2)_L$ for weak, and $U(1)_Y$ for QED. The Lagrangian has to be invariant under gauge transformation which results in all the particles being massless. In contrast to that, we observed the particles to be massive. They break gauge invariance. So an additional field called the Higgs field has been introduced to solve this problem. The Higgs mechanism involves two complex scalar fields in a weak isospin doublet.

$$\phi = \begin{pmatrix} \phi^+ \\ \phi^0 \end{pmatrix} = \begin{pmatrix} \phi_1 + i\phi_2 \\ \phi_3 + i\phi_4 \end{pmatrix} \tag{2.6}$$

Lagrangian for these fields are given as,

$$\mathcal{L} = (\partial_\mu \phi)^\dagger \partial^\mu \phi - V(\phi) \tag{2.7}$$

Potential $(V(\phi))$ is defined as,

$$V(\phi) = \mu^2 \phi^\dagger \phi + \lambda (\phi^\dagger \phi)^2 \tag{2.8}$$

The potential is required to have a finite minimum, called a vacuum state, therefore it is set to $\lambda > 0$. However μ can be chosen to be either $\mu^2 > 0$ or $\mu^2 < 0$. If $\mu^2 > 0$ is chosen, the single vacuum state of the potential is at the origin and from that point, the potential is symmetric in all directions.

This changes when $\mu^2 < 0$ is chosen because now the potential has acquired an infinite number of vacuum states at a distance v from the origin. At the origin, the potential is

---

[1]The choice of usage of down-type quarks in the definition is a convention. Other conventions are equally valid.

not at the minimum. It has a Mexican hat shape which can be seen in figure 2.2. From the point of any of those vacuum states the potential is not symmetric anymore and the symmetry is broken. Writing the Lagrangian at any one point where the potential is zero, one obtains terms that describe a Higgs boson and its interactions [21]. Expanding the
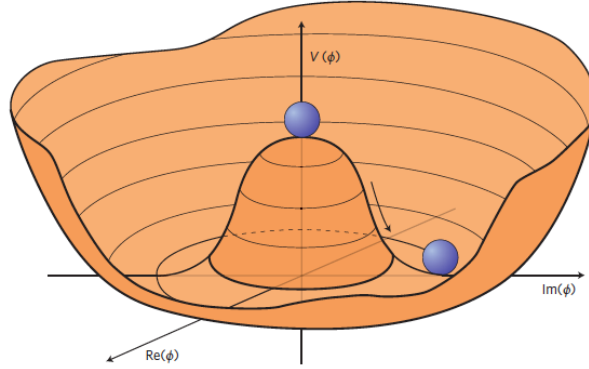

Figure 2.2.: The shape of the Higgs potential for one complex scalar field.

potential from a non-zero minimum, one can obtain a massive particle and three massless particles called Goldstone bosons. These massless particles disappear and interaction terms between the new massive field and the gauge bosons are found when the unitary gauge is applied. The coupling is given by the mass of the gauge bosons. These terms make the Lagrangian gauge invariant.

Though the fermion mass terms are gauge invariant, the masses are introduced in an ad-hoc manner. Fermion masses are explained via the Yukawa coupling. Yukawa couplings encode the interaction between the fundamental fermion fields and the Higgs field. The masses of fermions are introduced in the Lagrangian by:

$$
\begin{aligned}
\mathcal{L}_{Mass} = &-\frac{\sqrt{2}}{v}\left[(\bar{\nu}_L, \bar{e}_L)\phi M^e e_R + \bar{e}_R \bar{M}^e \bar{\phi}\begin{pmatrix}\nu_L \\ e_L\end{pmatrix}\right] \\
&-\frac{\sqrt{2}}{v}\left[(\bar{u}_L, \bar{d}_L)\phi M^d d_R + \bar{d}_R \bar{M}^d \bar{\phi}\begin{pmatrix}u_L \\ d_L\end{pmatrix}\right] \\
&-\frac{\sqrt{2}}{v}\left[(-\bar{d}_L, \bar{u}_L)\phi^* M^u u_R + \bar{u}_R \bar{M}^u \bar{\phi}^T\begin{pmatrix}-d_L \\ u_L\end{pmatrix}\right],
\end{aligned}
\tag{2.9}
$$

where $\bar{M}^e$ gives the mass parameters for leptons (electrons, muons, and taus), $\bar{M}^d$ gives for down type quarks and $\bar{M}^u$ gives for up type quarks summed over all three generations.

The coupling is linearly proportional to the fermion mass. The coupling is given by,

$$g_{coupling} = \frac{\sqrt{2}}{v} \times m_{Fermion} \tag{2.10}$$

where v is the vacuum expectation value. So the top quark couples most strongly to the Higgs boson.

The SM Higgs boson was discovered in 2012 at the LHC by the ATLAS [8] and the CMS [9] experiments using the $Z^0 Z^0 \to 4l$, $WW \to e\nu\mu\nu$, and $\gamma\gamma$ decay channels. The mass of the Higgs boson is 125.10 ± 0.42 GeV [22, 23]. The Higgs boson is a spin 0 and CP even particle [24, 25] with a lifetime of $\tau_{higgs} \approx 10^{-22}$ s [16].

2.3. The Top Quark

The top quark is the heaviest known fundamental particle with an mass of 172.76 ± 0.3 GeV[2]. It is a spin 1/2 particle with a charge of $+2/3$e. The top quark was discovered in 1995 at the Tevatron in the DØ and CDF experiments in proton-antiproton collisions [26, 27]. The existence of the top quark was postulated by Kobayashi and Maskawa in 1973 [28]. The top quark and its down-type counterpart, the bottom quark, complete the third generation of quarks. The top quark was discovered 18 years after the discovery of the b quark, as the top quark was heavier than anticipated and the required energy was not available at that time [26, 27].

Top quark pairs (top and anti-top) are produced via the strong force. Single top quarks are produced via the weak force. The production of top quark pairs is possible via $q\bar{q}$ annihilation or gluon-gluon fusion. Feynman diagrams of the top quark production are shown in figure 2.3.
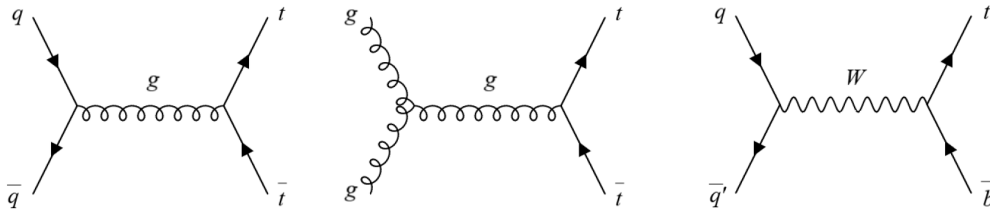

Figure 2.3.: (Left) Production of the top quark via $q\bar{q}$ annihilation. (Middle) Production of the top quark pair via gluon-gluon fusion. (Right) Production of single top quark via the weak process.

The mass of the top quark makes it an interesting particle as its mass is close to the electroweak scale and corresponds to a high Yukawa coupling in the order of 1. Due to its heavy mass, it has a very short lifetime of 10^{-25} s. Hence it decays before it can hadronise[2]. The top quark decays almost exclusively into a b quark and W^+ boson ($|V_{tb}| = 1.019 \pm 0.025$) [16], whereas the anti-top quark decays into an anti-b quark and a W^- boson. Decay channels of top quark pairs are determined by the decay of the W bosons. The W boson can decay hadronically or leptonically. In the all hadronic decay (6 jets) of the top quark - the top quark decays to two b jets and 4 additional jets from both W bosons, in the semi-leptonic decay - a charged lepton and a neutrino (observable by missing transverse energy) from one W boson and the other W boson decays hadronically

---

[2]Typical time period of hadronisation for heavy quarks is 3 fm/c [29] (1 fm/c $\sim 3 \times 10^{-24}$s).

and in a dileptonic decay, where both bosons undergo leptonic decays. The resulting branching ratio of the decay channels are depicted in figure 2.4).

Top Pair Branching Fractions

"alljets" 46%

τ+jets 15%

τ+τ 1%
τ+μ 2%
2%
τ+e 2%
1%
μ+μ 2%
μ+e 1%
e+e
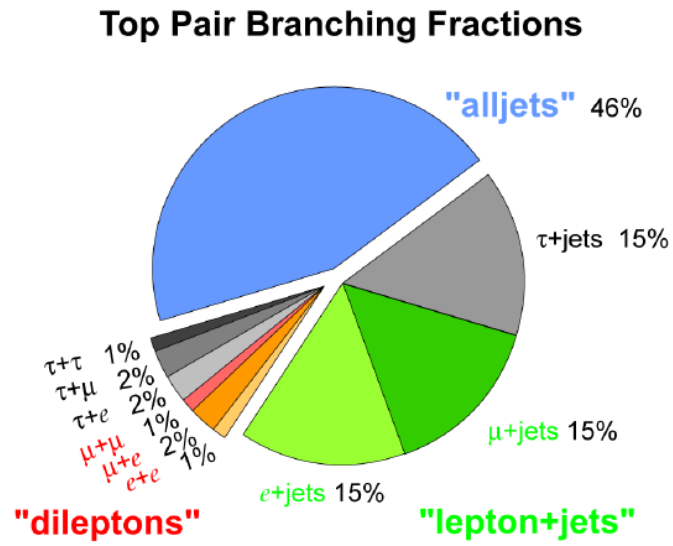
μ+jets 15%

e+jets 15%

"dileptons"

"lepton+jets"

Figure 2.4.: Top quark decay channels, depending on the W boson decay.

2.4. Physics Beyond the Standard Model

There are limitations of the SM. Gravity and dark matter is not included in the SM. All these are not explained by the SM, making it incomplete.

The SM predicts that the electroweak coupling of the gauge bosons to leptons is independent of lepton flavour. As a result, the ratio of the decay rate of W bosons to electrons and muons is expected to be unity. Previous measurements showed a consistent result in support of lepton universality [30].

In the SM, B-mesons decay to K-mesons, $\bar{b} \longrightarrow \bar{s}$ is suppressed but new physics predicts virtual particles that allow this transition. Feynman diagrams of these interactions are shown in figure 2.5.
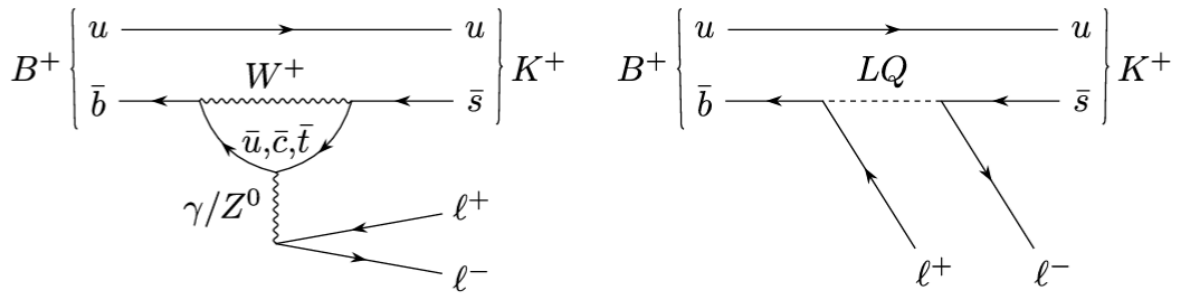
Figure 2.5.: (Left) The SM contribution involves the electroweak bosons γ, W^+, and Z^0. (Right) A possible new physics contribution to the decay with a hypothetical leptoquark (LQ), which, unlike the electroweak bosons, could have different interaction strengths with the different types of leptons [13].

A new measurement by LHCb presented the evidence with 3.1 standard deviations on breaking lepton universality. The measurements are of processes in which a beauty meson transforms into a strange meson via the emission of either an electron and a positron, or a muon and an anti muon [13].

By measuring the ratio of B-meson decay to K-mesons over the branching fractions, the measured double ratio of the decay is [13]

$$R_K = \frac{BR(B^+ \to K^+\mu^+\mu^-)}{BR(B^+ \to J/\Psi(\to \mu^+\mu^-)K^+)} \Big/ \frac{BR(B^+ \to K^+e^+e^-)}{BR(B^+ \to J/\Psi(\to e^+e^-)K^+)} = 0.846^{+0.044}_{-0.041}$$

(2.11)

Here $B^+ \to K^+l^+l^-$ decays are referred to as non-resonant whereas the $B^+ \to J/\Psi(\to l^+l^-)K^+$ are resonant decays. However, this is not enough to claim a discovery. If it breaks universality with 5 standard deviations, it implies effects Beyond the Standard Model (BSM).

My project is to study the BSM models that can lead to the electron-muon lepton universality violation in leading order (LO) top pair decay using the Monte Carlo (MC) simulation. My project focuses on the semi-leptonic decay of the top quark pair in 13 TeV collisions with the ATLAS experiment. The study is focused on models of new physics.

In this analysis, the BSM models such as W', Leptoquark, and charged Higgs boson are studied. W' is a hypothetical gauge boson named in analogy to the Standard Model W boson. Leptoquarks are hypothetical particles that would interact with quarks and leptons [16][31]. They are color-triplet bosons that carry both lepton and baryon numbers. Charged Higgs is a hypothetical boson predicted in 2 Higgs - Doublet model (2HDM) extension of the SM. A detailed description of these particles in the BSM models is given in Chapter 4.

3. The experimental setup

The experimental setup is described in this chapter. It is based on the ref. [32]. An overview of the ATLAS detector in the Large Hadron Collider (LHC) is given in section 3.2.

3.1. The Large Hadron Collider

The LHC [33] is currently the largest and most powerful proton-proton collider in the world built by the European Organization for Nuclear Research (CERN). It lies beneath the France-Switzerland border near Geneva. It is a 27-kilometer ring of superconducting magnets with several accelerating structures to boost the energy of the particles along the way. The protons are collided with a centre-of-mass energy of $\sqrt{s} = 13$ TeV. The CERN complex (see figure 3.1) consists of 4 interaction points where the protons collide - ATLAS [32], ALICE [34], LHCb [35], and CMS [36].
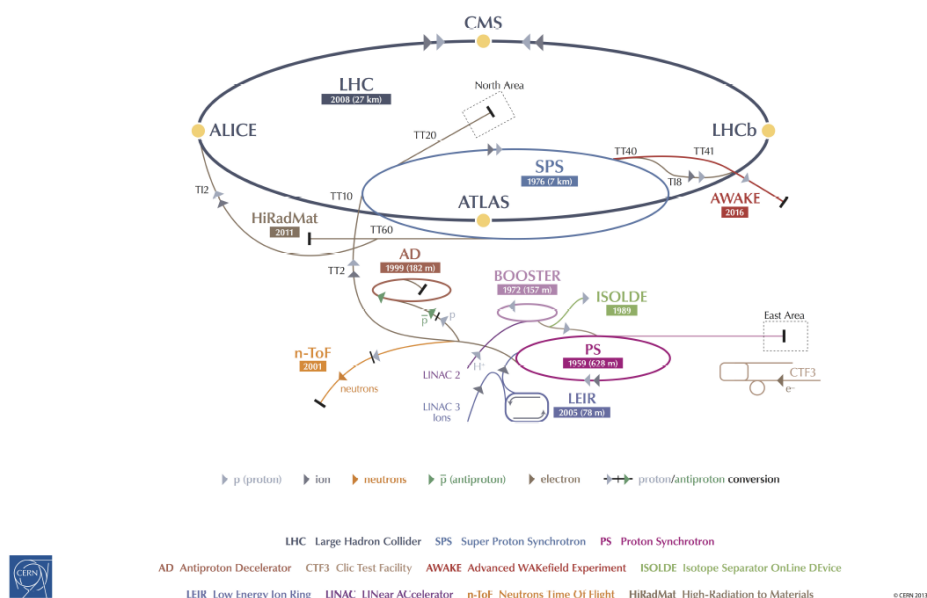

Figure 3.1.: The accelerator complex at CERN. Copyright: CERN.

3. The experimental setup

The LHC is currently recording the data for Run 3. The data-taking period for Run 3 is 3 years, from 2022 to 2025. Later from 2026, the LHC will be upgraded to the HL-LHC [37] to increase its luminosity and centre-of-mass energy. The upgrade of the LHC to a High Luminosity phase (HL-LHC) at 14 TeV center-of-mass energy with 3000 fb^{-1} of integrated luminosity will probe the Standard Model with even higher precision and could extend the sensitivity to possible anomalies in the Standard Model [38]. The sensitivity to find new physics Beyond the Standard Model (BSM) is significantly improved and could allow extending the reach for SUSY, heavy exotic resonances, vector-like quarks, dark matter, and exotic long-lived signatures, to name a few [39].

Luminosity gives the measure of how many collisions are happening in a particle accelerator. For N, the number of events for a certain process with a given cross-section σ and integrated luminosity $\int \mathcal{L} \, dt$ is given by

$$N = \sigma \int \mathcal{L} dt \,.$$
(3.1)

3.2. The Atlas detector
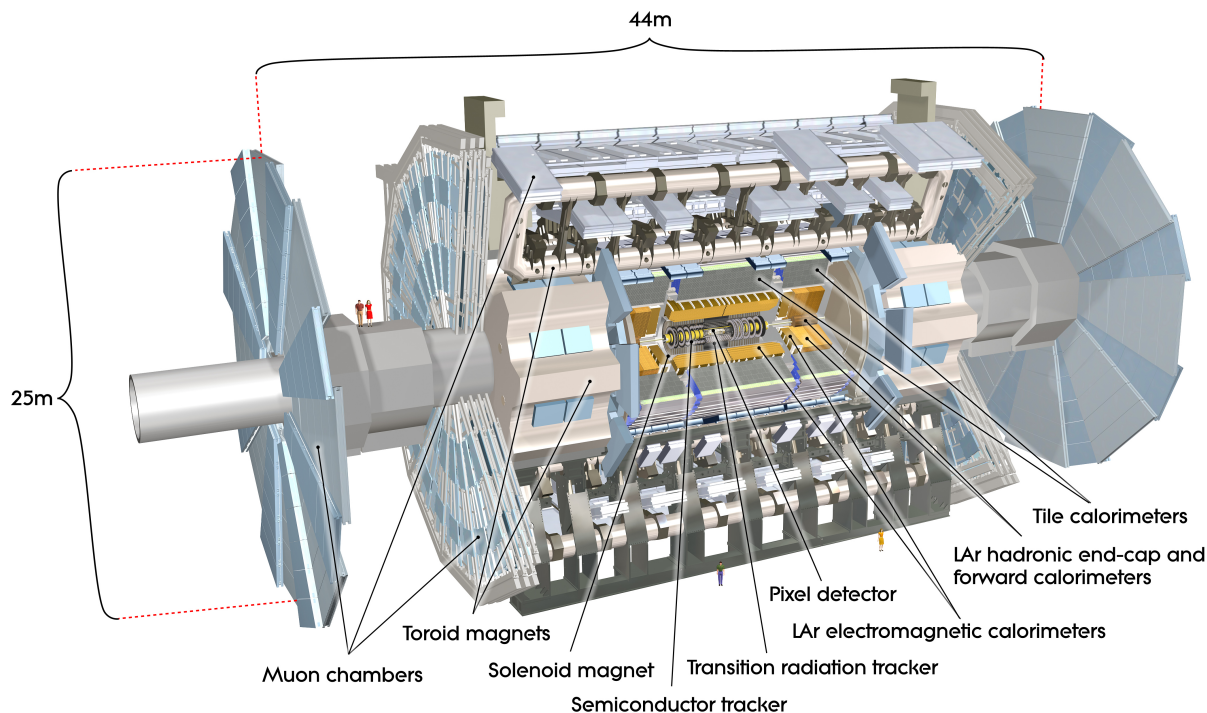
Figure 3.2.: The full ATLAS detector with all its components [32].

3.2.1. The ATLAS coordinate system

In the ATLAS detector, the collision point is considered to be the origin of the coordinate system. Since the detector is cylindrical in shape, cylindrical coordinates are used as the coordinate system. The beamline is the z-axis. The x-axis points to the centre of the LHC and the y-axis points upwards. The azimuthal angle ϕ is between the x and y axes. The polar angle θ is defined as the angle from the positive z-axis. From the polar angle, which is the angle between the z-axis and the outgoing particle, the pseudorapidity η is determined $\eta = -\ln\tan\left(\frac{\theta}{2}\right)$ [32].

3.2.2. Detector components

The ATLAS detector (**A T**oroidal **L**HC **A**pparatu**S**) is the largest particle detector located at the LHC. It has a cylindrical structure with a length of about 44 m and 25 m in diameter. It is a multipurpose experiment with a typical onion structure and covers

nearly the full solid angle as shown in figure 3.2. The detector is divided into a barrel part and an end cap part. The tracking detector is centred nearest to the beam pipe. It is enclosed by a solenoid magnet of 2 T. It measures the tracks of charged particles and their momentum. It has three innermost sub-components. They are the insertable B-layer (IBL), the silicon pixel detector, and the semiconductor tracker (SCT).

The next part is the calorimeter. The two calorimeters are placed as follows, electromagnetic calorimeter (ECAL) and then the hadronic calorimeter (HCAL). This measures the particle energy. The particles deposit energy in the active material of the calorimeter which is then measured. The electromagnetic (EM) calorimeter contains barrel and end cap parts. Liquid Argon (LAr) is used in the EM calorimeter as active material. Electrons deposit energy by Bremsstrahlung and electron-positron pair production.

The hadron calorimeter comes next. It measures the deposited energy of hadrons. It contains a barrel, end cap, and a forward calorimeter. The barrel is in the central region of the detector. Iron and plastic scintillators are used as absorber and active material. End-caps use copper as an absorber and liquid Argon as active material, respectively. Enclosing the end cap is the forward calorimeter. Liquid argon is used as active material.
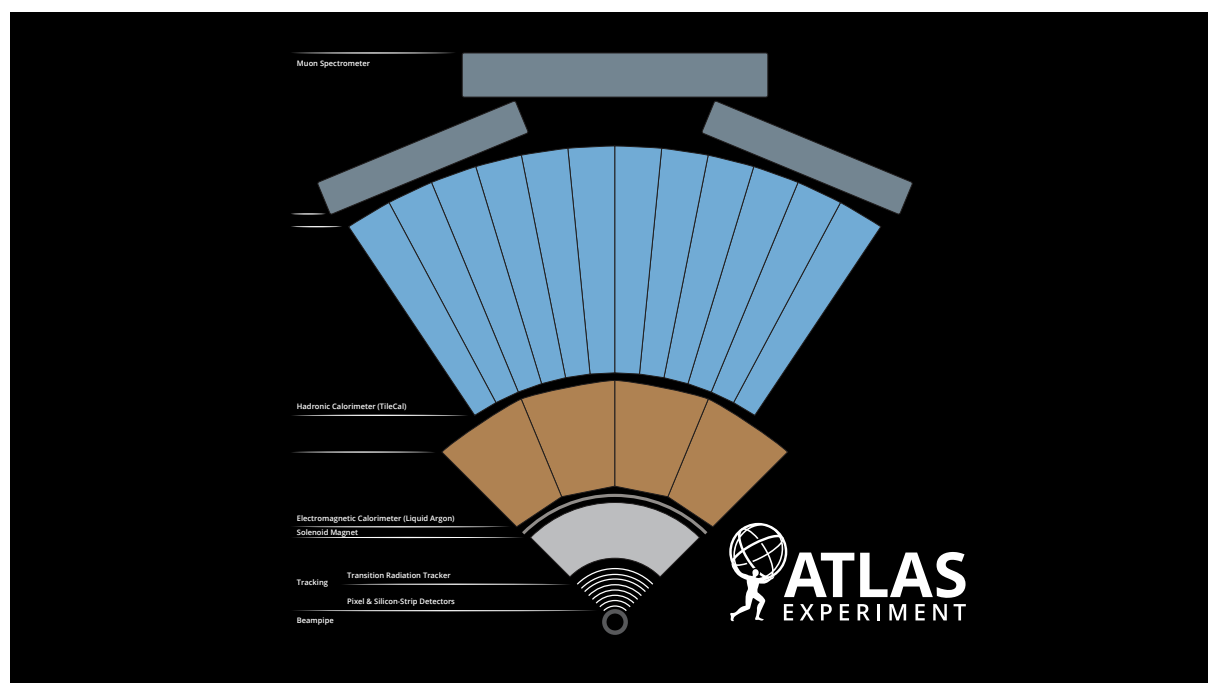

Figure 3.3.: Cross-sectional view of ATLAS detector copyright: CERN.

A jet is a cone of hadrons and other particles. Since jets comprise multiple particles, multiple tracks in the detector are included. The jet reconstruction is done by matching preselected tracks with one topological cluster. The clustering is done with the anti-k_t algorithm [40].

Muons are heavy and they cross the EM calorimeter. They pass to the muon spectrometer. It is equipped with a toroidal magnet that bends the trajectory of muons. The muon spectrometer measures the momentum of muons. Its field strength varies in the barrel region from 0.15 T to 2.5 T and in the end cap from 0.2 T to 3.5 T. A cross-sectional view of the Atlas detector is shown in figure 3.3. The transverse momentum, energy resolution, and η coverage of Atlas detector components are shown in table 3.1.

Component	Resolution (GeV)	η coverage
Inner Detector	$\frac{\sigma_T}{P_T} = 0.05\% \cdot P_T \oplus 1\%$	$\pm\,2.5$
ECAL	$\frac{\sigma_E}{E} = 10\%/\sqrt{E} \oplus 0.7\%$	$\pm\,3.2$
HCAL (barrel and end cap)	$\frac{\sigma_E}{E} = 50\%/\sqrt{E} \oplus 3\%$	$\pm\,3.2$
HCAL (forward calorimeter)	$\frac{\sigma_E}{E} = 100\%/\sqrt{E} \oplus 10\%$	$3.1 < \eta < 4.9$
Muon Spectrometer	$\frac{\sigma_T}{P_T} = 10\%$ at $p_T = 1000$	$\pm\,2.7$

Table 3.1.: Transverse momentum and energy resolution of the Atlas detector components as well as their η coverage [32].

3.2.3. The Trigger system

At the Lhc, the collision rate of particles is very high, approximately 40 MHz. Not all the data can be stored. Hence, a filter is required to keep interesting events. For this purpose of filtering interesting events, a trigger is used. A two-trigger system is implemented [41]. The level 1 trigger is hardware based. It builds regions of interest (RoI) and passes these on to the second level. Now the reduced rate is 100 kHz. The second level is a high-level trigger (HLT) which is software based. It can further reduce the rate to about 1 kHz.

4. Simulation and Analysis

4.1. Simulation

Simulation of events plays a pivotal role in estimating the signal sensitivity of a process. Studying the different kinematic variables provides an estimate of the expected outcome. There are many matrix element generators and parton shower algorithms that can be utilised.

This analysis uses MadGraph_aMC@NLO [42] [43] as its Monte Carlo generator to generate events. It is a framework that aims at providing all the elements necessary for SM and BSM phenomenology, such as the computations of cross sections and the generation of hard events. Alongside Leading order (LO) it can also generate at tree and one loop level. LO corresponds to the lowest order in couplings at which a process can occur. MadGraph can be used within Athena [44], the ATLAS software framework that manages almost all ATLAS production workflows: event generation, simulation, reconstruction, and derivation production. Athena is also used online in the ATLAS High-level Trigger. The Monte Carlo (MC) generation has job options as input that contain the process ID and relevant parameters for the process such as masses of particles involved, coupling parameters, decay width, etc. The job options can be run with a python script. MadGraph provides the options to modify those parameters. The generated event information is stored in a root file. ROOT [45] is a software framework for data analysis. It is an object-oriented program and library developed by CERN.

The generated events are then analysed using the RIVET toolkit [46]. RIVET (**R**obust **I**ndependent **V**alidation of **E**xperiment and **T**heory) is a system used for the validation of Monte Carlo event generators. It provides a large set of experimental analyses for MC generator development, validation, and tuning. It reads the generated input data from the MC simulations based on the analysis selected. It can also produce comparison plots with published data [46] and generate the output in formats such as root files or yoda files. Yoda files are simple, readable text files that contain the histograms from the analysis. It

is used to produce plots easily and efficiently.

4.2. Analysis

Violation of lepton universality implies effects Beyond the Standard Model. BSM models that can lead to the explanation of possible lepton universality violation in top quark decays are studied using the Monte Carlo (MC) simulation of top quark decay events. MC events are generated with MadGraph5_aMC@NLO (AthGeneration 21.6.80) [43] within the Athena framework and are then analysed using the RIVET toolkit. The study is focused on the single-lepton channel of the $t\bar{t}$ pair decay. In Rivet, at the particle level, electrons and muons are similar. Only in the detector they look very different. The difference between them is experimental rather than fundamental. This analysis focuses on the BSM affects that can affect the measured muon over electron ratio. The effects could be on either of the channel or both. So, either channel can be chosen for the study. It is arbitrary. Here, the muon channel is considered.

For event generation, a UFO (Unified FeynRules Output) model containing the simplified models of vector leptoquarks (particles that interact with quarks and leptons) and gauge bosons (W') is used.

They are:

- A simplified model with a spin-1 W' boson coupling differently to different quark and lepton generations.

- A simplified model with a leptoquark coupling differently to different quark and lepton generations.

- The interference effects between SM and BSM are ignored.

A 2HDM type-II model is used for the generation of the charged Higgs boson events. For the analysis of the generated events, a custom Rivet routine with the selection mimicking the cuts in the measurement is used.

- Jet p_T >25 GeV, η <2.5

- Lepton p_T >27 GeV, η <2.5

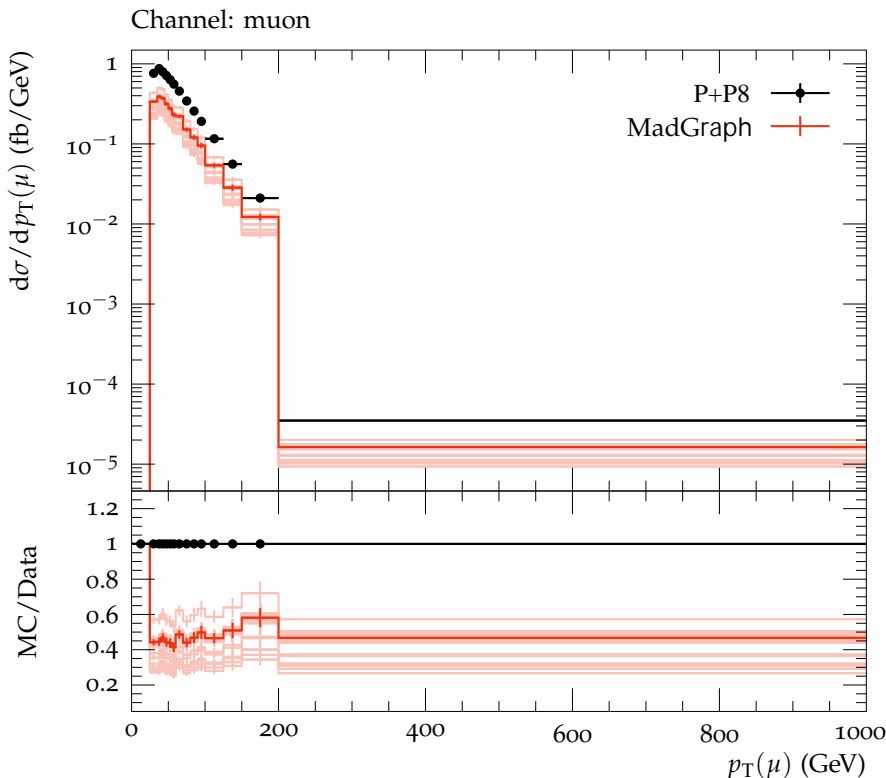- Total number of jets >3 (3 b jets)

Figure 4.1.: Comparison of Powheg+Pythia 8 sample to the generated SM MC events (MadGraph) in muon p_T distribution.

Generated events are normalised to ensure the correct luminosity scaling in the UFO model. Nominal $t\bar{t}$ samples are produced with Powheg+Pythia 8 (DSID[1] = 410470). The nominal sample contains the $t\bar{t}$ events with non-all hadronic decay channels. The SM MC events for the top pair decay to a single leptonic muon channel are generated. The expected cross section at LO for this process is ~ 52.4 pb. Then the generated events are plotted using Rivet. Figure 4.1 shows the comparison of the Powheg+Pythia 8 events to the generated MC top pair decay in the semi-leptonic muon channel.

The muon p_T distribution shows the expected behaviour. There is a small mismatch between the Powheg+Pythia 8 (P+P8) sample and the generated MC top pair decay in the semi-leptonic muon channel. The P+P8 sample contains all non-hadronic decays of top pairs i.e., $\sim 56\%$ of top decay (see figure 2.4). It also contains NLO processes (Next-to-the-Leading Order) but the generated MC events are of LO. The difference gives a k-factor of approximately 15%. In the Rivet analysis, the selection of the muon channel (single-leptonic) events is about 15%. Minor fractions of dileptons and Taus also pass the

---

[1]DSID - Dataset ID

cut (around 10%). All this causes distributions to be different between the generated MC and P+P8 sample. All together explains the ∼40% mismatch between the generated MC and P+P8 sample. It can be seen in figure 4.1. Black dots is the Powheg+Pythia 8 simulated events and the red points is the generated MadGraph events.

For the analysis with the BSM models, P+P8 is not used as the events in the P+P8 are NLO processes but the generated BSM events are of LO processes. So, the events are generated for the SM $t\bar{t}$ sample with MadGraph instead of using the P+P8 events.

4.3. Folding

The simulated events can be classified into two types: particle level prediction and detector level events. Particle level prediction is the theoretical simulation of what an event could look like, without the detector effects. The detector level shows how the events are after the collisions in the detector, with the detector effects.

Monte Carlo simulation is done in a chain of processes starting with a physics model that describes the framework in which the calculations are performed (eg. the SM). By defining the initial, final state particles of the processes, and the order of calculation, the matrix element (ME) is automatically prepared. After the ME is integrated over the parameters' phase space, the code for an event generator is constructed that generates random samples for all final state physical particles [47]. In most analyses, the response of the particles to the detector is simulated with the Geant 4 framework [48].

However, simulating events for all the BSM models using the Geant 4 framework is expensive and time consuming. Hence in this analysis, the particle-level events are generated in MadGraph. As these particle-level events do not contain the detector effects, they cannot be compared directly to the detector level events. Detector effects need to be added using the "Response matrix". Now these events can be compared directly to the data. The generation of the events using MadGraph and applying the response matrix to obtain the detector level events consumes less time and resources compared to the Geant 4 framework.

Comparing these truth events to the detector level can be done by:

- Unfolding the data to remove detector effects from data and obtain a particle-level distribution, which is then compared with simulated particle-level predictions [49].

- Folding the particle-level prediction, by simulating the detector response to get a reco-level prediction and then comparing directly with the data.

In folding of the particle level prediction to the detector level or unfolding the detector level events to the particle level prediction, the response matrix plays a pivotal role. The response matrix is the combination of selection efficiency, migration matrix, and acceptance. It provides information about the detector effects.

Selection efficiency refers to the detector's effectiveness in finding objects which have passed through the detector. The migration matrix relates to the probability distribution of the "true" characteristic value to be measured as a different value and can be obtained with the MC simulation of detector response [50]. Acceptance refers to the geometric fiducial volume of the detector.

The distribution at the detector level is obtained by matrix multiplication of the particle level distribution with the response matrix.

Detector level (Reco level) = particle level prediction × Response matrix

Full detector simulation is an expensive process and there are potentially a very large number of BSM models to test. Instead of simulating them all, particle-level predictions are folded with the response matrix obtained from the simulated MC SM sample. Hence, the particle level events are reconstructed accounting for detector effects to reconstructed level and compared to the data events in the detector. This technique is called folding or convolution.

4.4. The W' model

The W' boson is a hypothetical particle of spin 1 and an electric charge of ± 1. It is a colour singlet particle [16]. The W' boson couples to both quarks and leptons. The mass limits on the W' boson are set based on its decay channel individually. Throughout this analysis, we are focused on the muon channel.

In the muon channel, ATLAS and CMS set mass limits for a W' mass in the 0.15-7 TeV range from the analysis based on 36-139 fb^{-1} at $\sqrt{s} = 13$ TeV [51][52], with the strongest lower limit on the mass of 5.1 TeV at 95% CL (confidence level) for the Sequential Standard Model (SSM) set by ATLAS [51] (shown in figure 4.2) using 139 fb^{-1} of $\sqrt{s} = 13$ TeV data. W' couplings to leptons are based on the SSM. The SSM is an extension of the SM of particle physics that predicts the existence of new resonances with properties similar to that of the SM. In the SSM, the couplings of W' bosons to the leptons are assumed to be the same as the couplings of the W boson to leptons in SM.
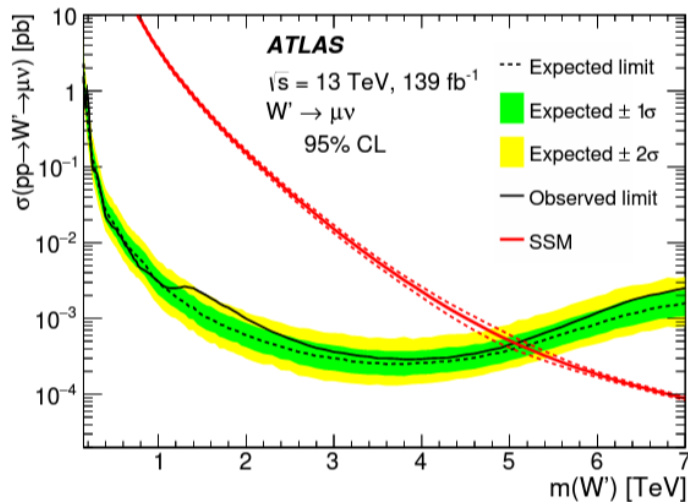

Figure 4.2.: Upper limit on $\sigma(\mathrm{pp} \to W'\,\mathrm{X}\,)\,\mathrm{B}(W' \to \mu\nu)$ as a function of the W' mass from ATLAS [51]. The red line shows the theoretical prediction in the Sequential SM.

ν In the model considered in this analysis, the coupling parameters of W' to leptons and third generation quarks are set to non-zero values. The rest of the couplings are zero. The resulting $t\bar{t}$ pair decay is one (anti) top quark decays to a (anti) bottom quark and a W' boson while the other decays as predicted by the SM (see in figure 4.3). Subsequently, the W' boson decays to a lepton and its neutrino. Since the study is focused on the muon channel, only W' couplings to a muon and its neutrino are set to non-zero. Hence in this model, the W' boson decays to the second generation lepton pair only.
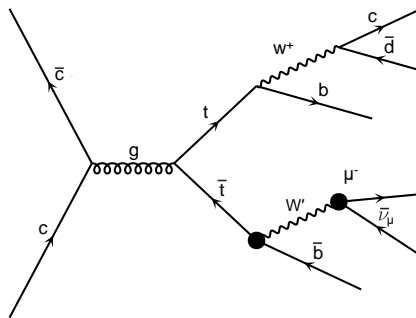

Figure 4.3.: Feynman diagram representing a W' boson interaction in a top quark decay.

On-shell $t\bar{t}$ events are generated by the MadGraph5_aMC@NLO [2] [43] generator within the Athena framework and interfaced with Pythia 8 (v.245) [53] to simulate parton showers. EvtGen (v.1.7) was used to simulate (b-)hadron decays. The W' boson mass range considered for the study from 10 GeV to 180 GeV. We focus on the lower mass range and non-SSM coupling parameters for the W' as the current dedicated searches focus in the phase space of high energetic W' with the SSM-like coupling parameters. The observed cross section exhibits an exponential decrease (figure 4.4) as the W' boson mass increases.

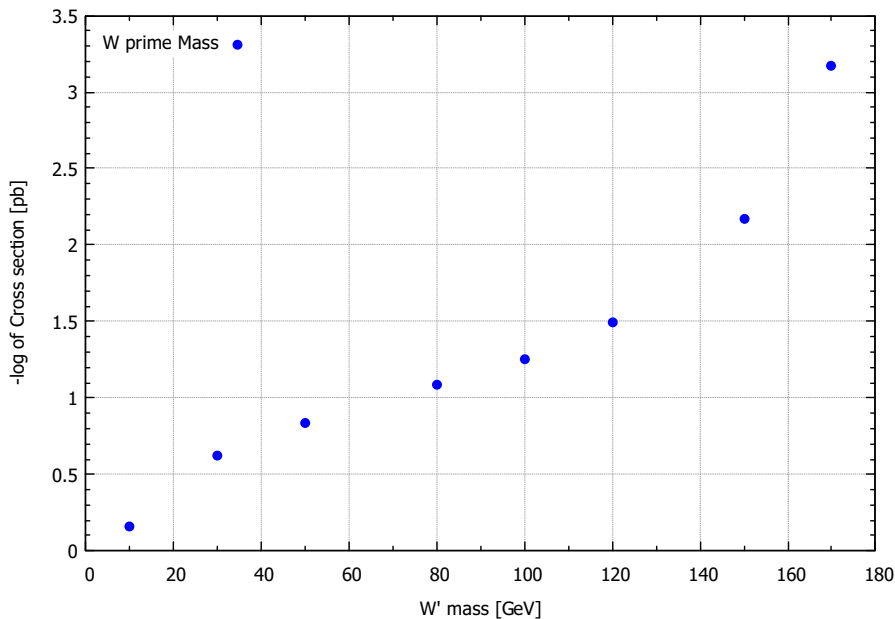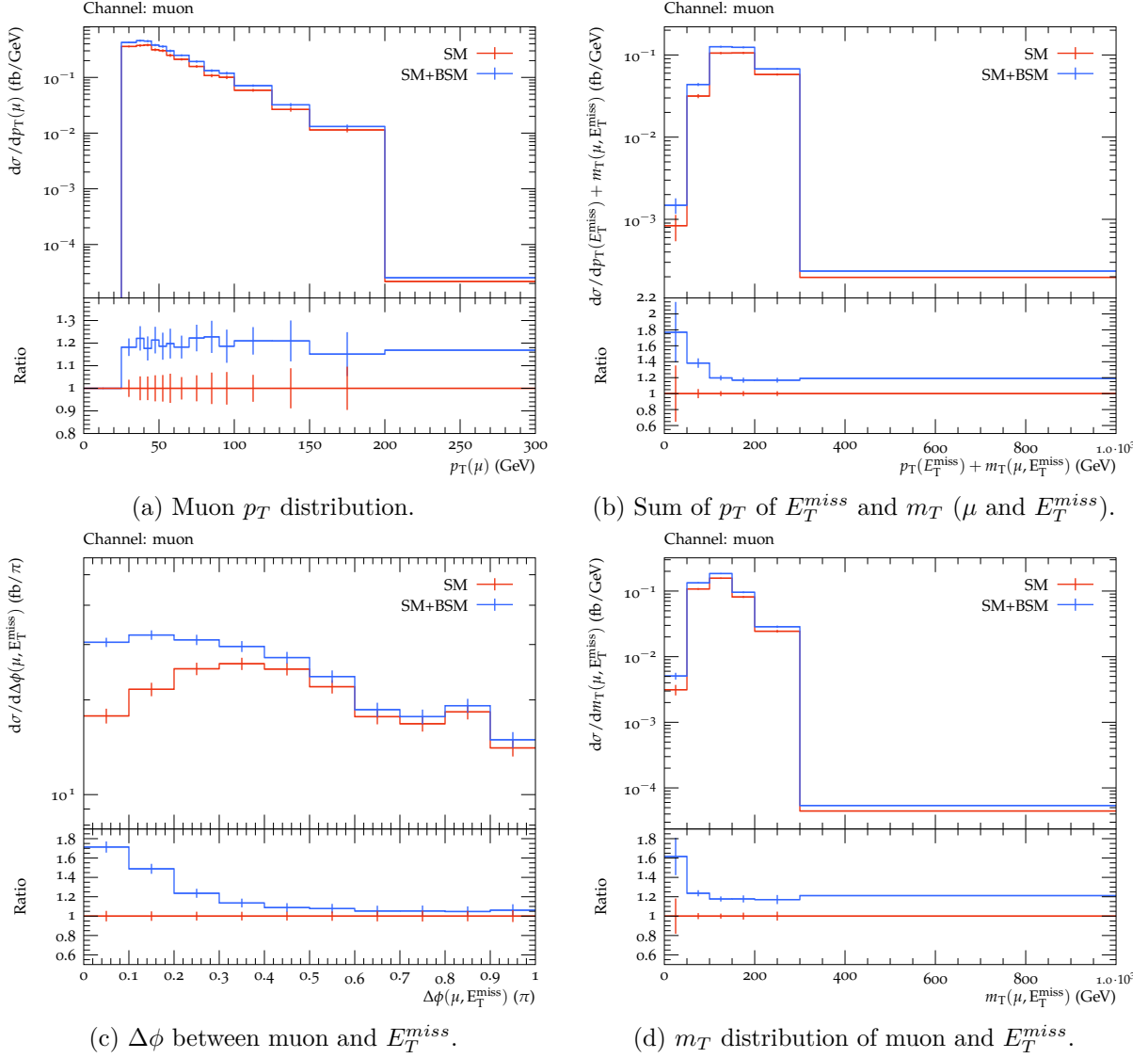[2]For detailed changes to the job options to run in MadGraph see A.1

Figure 4.4.: Logarithmic scale of Cross section as a function of W' mass.

In this model, the W' boson coupling to the leptons is an arbitrary constant. The BSM shape effects on different kinematic variables are observed by changing the mass of the W' boson which are then compared to the distribution of variables in the SM. For the clear comparison of shapes of the kinematic variables between the W' masses, the coupling constant is set such that the cross section of the W' production is 20% of the SM cross section.

Differential cross sections of various kinematic variables were studied to find the variables that show a difference with respect to the Standard Model. Primary variables of interest are the lepton transverse momentum (p_T), defined as $p_T = \sqrt{p_x^2 + p_y^2}$, where p_x and p_y are the momentum components in the transverse momentum plane; missing transverse energy (E_T^{miss}); corresponding to the energy that is not detected in the detector but is expected due to the laws of conservation of energy and momentum; transverse mass (m_T) for a two body decay of W' boson into a lepton and neutrino (MET), defined as $m_T = \sqrt{2p_T^l E_T^{miss}(1 - cos\phi)}$, where p_T^l is the transverse momentum of the lepton and ϕ is the opening azimuthal angle between the charged lepton and the missing transverse momenta.

4.4.1. W' mass - 30 GeV

(a) Muon p_T distribution.

(b) Sum of p_T of E_T^{miss} and m_T (μ and E_T^{miss}).

(c) $\Delta\phi$ between muon and E_T^{miss}.

(d) m_T distribution of muon and E_T^{miss}.

Figure 4.5.: Distributions of kinematic observables for the W' boson of mass 30 GeV.

The ratio between the BSM and the SM distributions is plotted to show the shape effects. It is taken between the SM events and the sum of the SM and the BSM events. The rest of the plots shown in this study also show the $\frac{\text{SM+BSM}}{\text{SM}}$ ratio unless explicitly specified otherwise. The red line denotes the SM distributions and the blue line denotes the sum of the SM and the BSM events.

Muon transverse momentum (p_T) distribution is shown in figure 4.5(a). For a W' of 30 GeV mass, the ratio plot for lepton momentum distributions shows no significant shape difference with the SM. Considering the statistical fluctuations (Poisson errors) the shapes
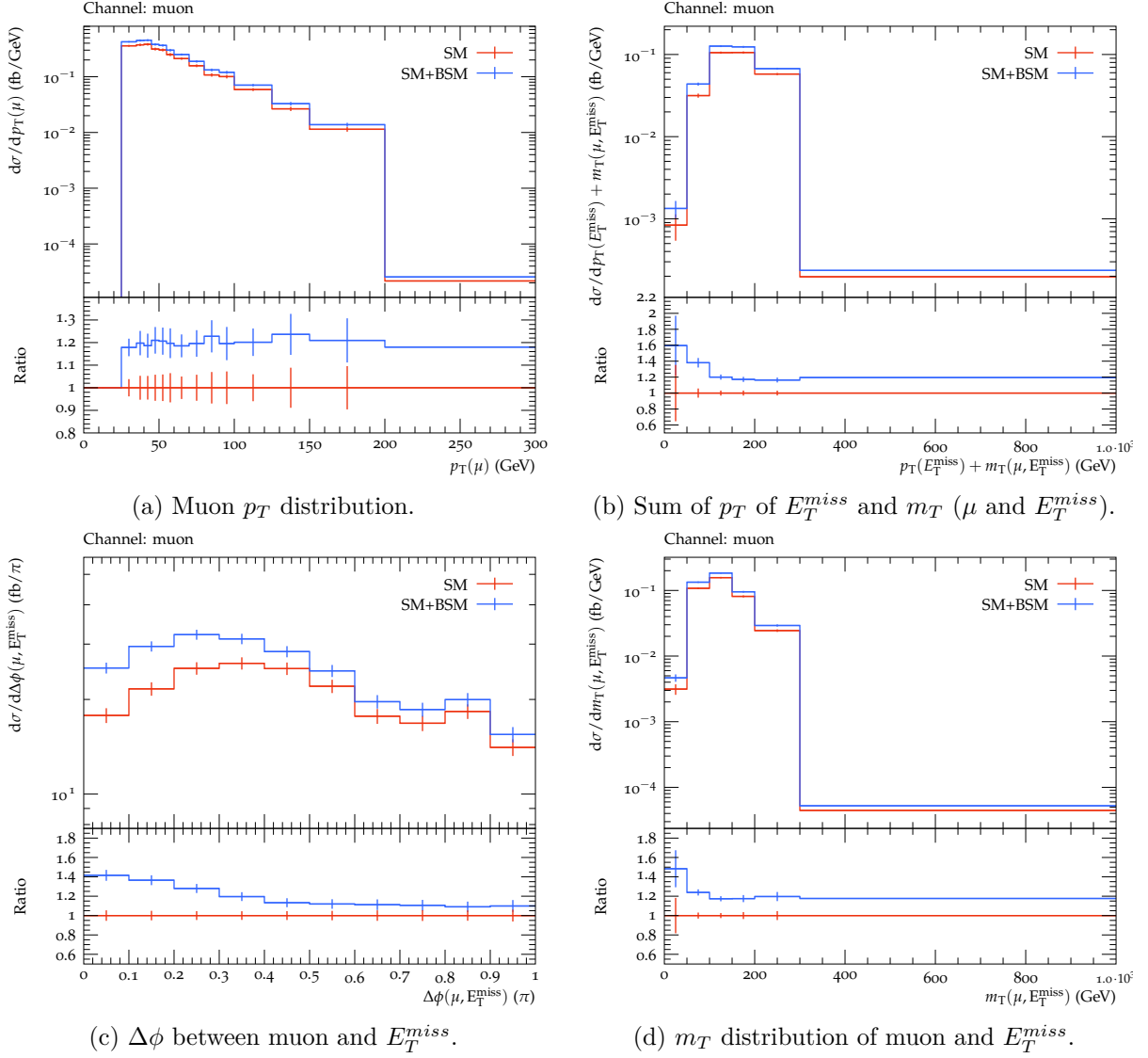
4. Simulation and Analysis

of lepton momentum are similar.

The shape of the sum of the transverse mass of muon and MET, and transverse momentum of E_T^{miss} variable is similar except for the first bin. The difference in the first bin of the sum of transverse mass and E_T^{miss} distribution is due to the lower mass of the W' than the W mass in SM which leads to softer transverse mass and E_T^{miss} distributions. The sum of the lepton p_T of E_T^{miss} and transverse mass of muon and E_T^{miss} is shown in figure 4.5(b).

$\Delta\phi$ is defined as the azimuthal angle between the muon and the MET. The larger number of events with low $\Delta\phi$ for a BSM distribution can be explained by lower W' mass so that the decay products of the boson do not have enough momentum to be separated. The $\Delta\phi$ distribution is shown in figure 4.5(c). As the boson mass increases more events are produced with larger $\Delta\phi$ [3]. The values of the transverse mass (m_T) of the lepton and the E_T^{miss} resulting from the decay of low mass W' boson is small as can be seen in figure 4.5(d).

---

[3]Evolution of the shape shift in $\Delta\phi$ distribution is shown in appendix B

4.4.2. *W'* mass - 50 GeV

(a) Muon p_T distribution.

(b) Sum of p_T of E_T^{miss} and m_T (μ and E_T^{miss}).

(c) $\Delta\phi$ between muon and E_T^{miss}.

(d) m_T distribution of muon and E_T^{miss}.

Figure 4.6.: Distributions of kinematic observables for the W' boson of mass 50 GeV.

The results for W' mass of 50 GeV are similar to that of W' with a mass of 30 GeV. The p_T distribution is shown in figure 4.6(a). Considering the statistical fluctuations in the p_T distribution the shapes of lepton momentum are similar to that of the SM. The sum of the m_T of muon and MET, and p_T of E_T^{miss} distributions have large number of events in the first bins compared to the last bins because of the low mass W' boson.

4. Simulation and Analysis

The $\Delta\phi$ distribution is shown in figure 4.6(c). The number of events in the lower bin of $\Delta\phi$ distribution (in figure 4.6(c)) is larger because of the lower W' mass. However, the excess of the events in the first bin is small compared to the $\Delta\phi$ distribution of the W' boson of mass 30 GeV (see figure 4.13). This is because of the increase of the W' boson mass from 30 GeV to 50 GeV. As the boson mass increases, many events are found towards the larger $\Delta\phi$. The W' boson has enough momentum for its decay particles to get separated in decay.

4.4.3. W' mass - 165 GeV

(a) Muon p_T distribution.

(b) Sum of p_T of E_T^{miss} and m_T (μ and E_T^{miss}).

(c) $\Delta\phi$ between muon and E_T^{miss}.

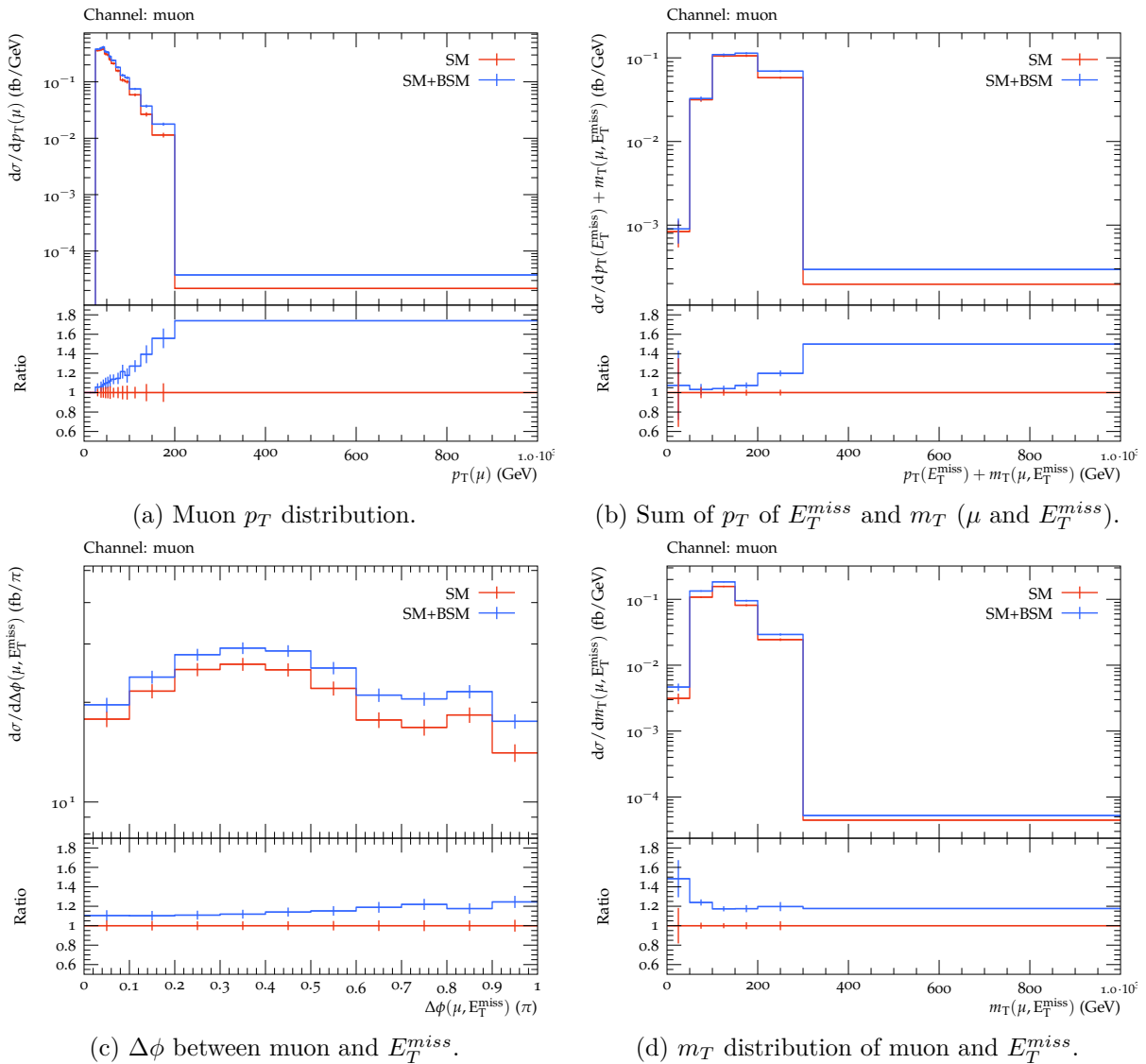(d) m_T distribution of muon and E_T^{miss}.

Figure 4.7.: Distributions of kinematic observables for the W' boson of mass 165 GeV.

For a W' mass at 165 GeV, the shape of the lepton p_T distribution deviates significantly from the SM. The statistical fluctuations are small and a clear difference is visible. As the W' mass approaches the top mass, lepton p_T in the decay becomes harder. Leptons with larger p_T are observed. A large number of events is observed in the high p_T bin (figure 4.7(a)). The shape in the sum of the transverse mass and the missing E_T and p_T variable distribution remains as expected. The distribution is shown in figure 4.7(b).

A large number of events in the last bin of $\Delta\phi$ distribution is observed because of the large mass of the W' boson. The decay products of the boson now have enough momentum to get separated. The $\Delta\phi$ distribution is shown in figure 4.7(c).

4. Simulation and Analysis

4.4.4. W' mass - 180 GeV

(a) Muon p_T distribution.

(b) Sum of p_T of E_T^{miss} and m_T (μ and E_T^{miss}).

(c) $\Delta\phi$ between muon and E_T^{miss}.

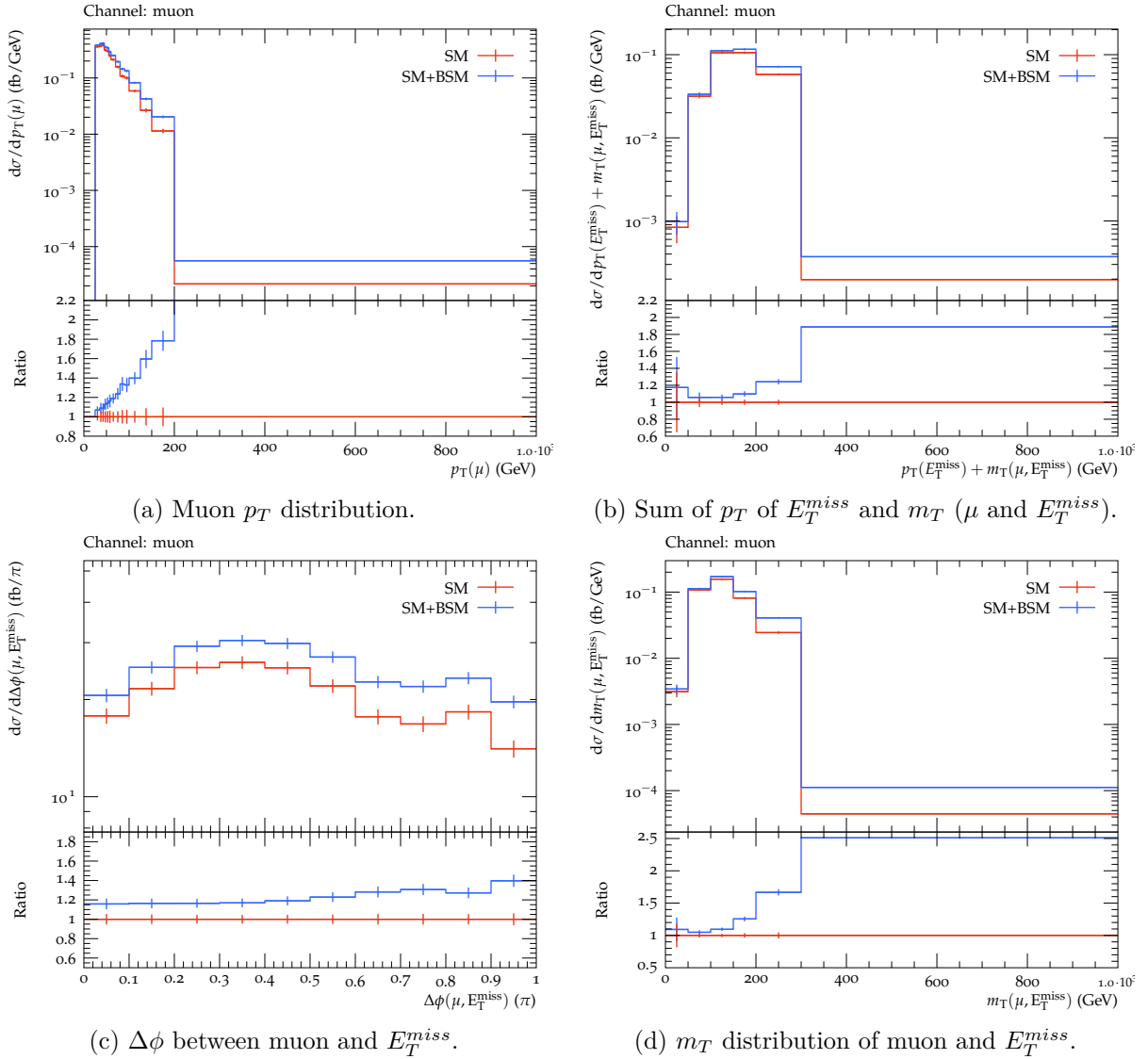(d) m_T distribution of muon and E_T^{miss}.

Figure 4.8.: Distributions of kinematic observables for the W' boson of mass 180 GeV.

In the SM, the top quark is the heaviest known particle. Hence, in an on-shell process, as the W' boson mass is set larger than the top mass, its production rate is heavily suppressed. The MC simulation shows the same trend as for a W' boson of mass 165 GeV. The largest difference between the SM and the BSM is visible in the high tails of all considered distributions shown in figures 4.8(a)-4.8(d). The trend of $\Delta\phi$ is observed over the W' masses of 30 GeV (figure 4.5(c)), 50 GeV (figure 4.6(c)), 165 GeV (figure 4.7(c)) and 180 GeV (figure 4.8(c)).

4.5. The Leptoquark model

Leptoquarks (LQ) are hypothetical particles that carry both lepton and baryon quantum numbers [54]. They couple directly to both quarks and leptons. They are colour triplet particles. A leptoquark with spin 0 is a scalar leptoquark (denoted by LQ_S) and with spin 1 is a vector leptoquark (denoted by LQ_V). In this analysis, vector Leptoquarks are generated. At the LHC, leptoquarks can be produced either in pairs or alone. Leptoquarks are divided into three generations depending on the generation of fermions they couple to. The first generation leptoquarks couple to the first generation of fermions, the second generation leptoquarks to the second generation of fermions, and the third generation of leptoquarks to the third generation of fermions. There are also transgenerational leptoquarks which couple in between the generations of the fermions. For i = quark generations and j = lepton generations, the transgenerational leptoquarks couple to a different generation of quarks and leptons (i $\neq$ j).

The most stringent current limits on the leptoquark pair production are from CMS. The analysis used proton-proton collision data at $\sqrt{s} = 13$ TeV, recorded with the CMS detector at the LHC in 2016. Leptoquarks of masses up to 1530 GeV are excluded assuming the Yang-Mills case with coupling $\kappa = 1$, or 1115 GeV in the minimal coupling case $\kappa = 0$ [55].

The single leptoquark production cross section depends on the Yukawa coupling, so the mass limits on the leptoquarks are displayed in a mass-coupling plane. For leptoquark Yukawa coupling $\lambda = 0.1$, early ZEUS Collaboration bounds on the first-generation leptoquarks range from 248 to 290 GeV, depending on the leptoquark species [56]. For coupling constant $\lambda = 0.3$, The H1 collaboration excluded leptoquarks with a mass up to 800 GeV at 95% CL [57]. Complementary to HERA, the CMS collaboration performed searches for single production of first and second generation leptoquarks [58] for coupling strength $\lambda = 1.0$, first generation leptoquarks are excluded for masses up to 1.73 TeV and second generation leptoquark are excluded up to masses of 530 GeV in proton-proton collisions at $\sqrt{s} = 8$ TeV.

In this analysis, the coupling parameters of LQs to leptons and quarks are set to non-zero values. The LQ decays to a lepton (either charged lepton or a neutrino) and a quark. In the $t\bar{t}$ pair decay, one (anti) top quark decays to a (anti) bottom quark and a leptoquark while the other decays via the Standard Model to a W boson (subsequently to hadrons (jets)) which can be seen in figure 4.9. Since the study is focused on the muon channel, only the leptoquark coupling to a muon and its neutrino are set to non-zero. Hence, in

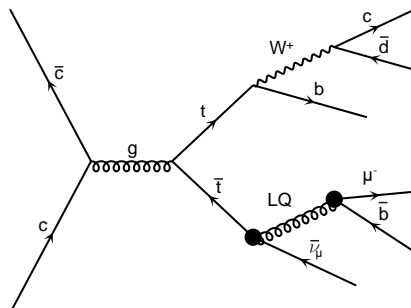this model, the leptoquark subsequently decays to the second generation lepton pair only.

Figure 4.9.: Feynman diagram representing a leptoquark interaction in a top quark decay.

On-shell $t\bar{t}$ events are generated by the MadGraph5_aMC@NLO [4] [43] generator within the Athena framework and interfaced with Pythia 8 (v.245) [53] to simulate parton shower. EvtGen (v.1.7) was used to simulate (b-)hadron decays. The leptoquark boson mass range considered for the study is 10 GeV to 170 GeV. The observed cross section exhibits an exponential decrease (figure 4.10) as the leptoquark boson mass increases. This analysis primarily focuses on the low mass leptoquarks, as the current direct searches cover the phase space of high energetic leptoquarks.
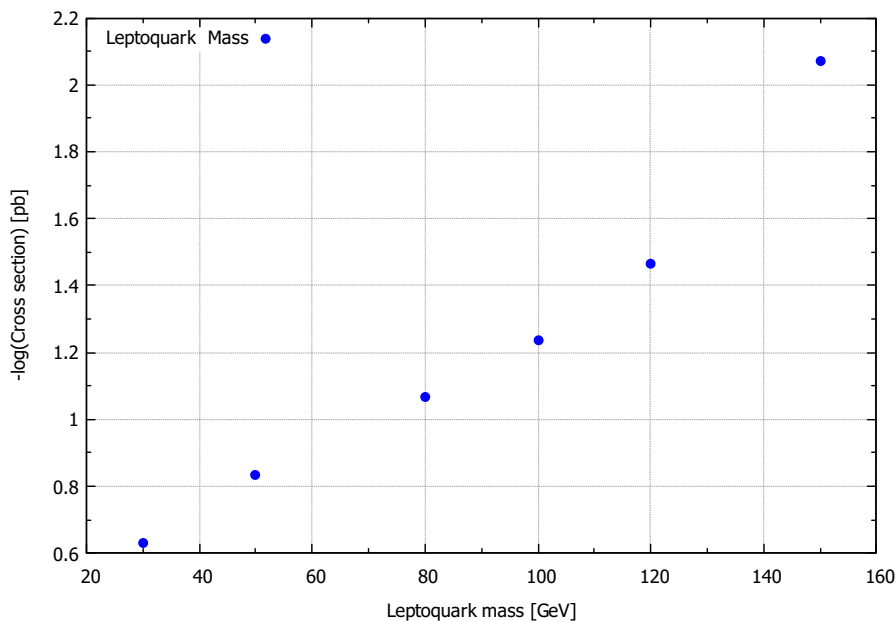

Figure 4.10.: Negative logarithmic scale of Cross section as a function of leptoquark mass.

In this model, the leptoquark coupling to the lepton and quarks is an arbitrary constant. For the analysis, the coupling constant is set to $\lambda = 0.1$. The BSM shape effects on different kinematic variables are studied by changing the mass of the leptoquark.

Depending on the charge of the LQ, it decays to either a charged lepton and a quark (LQ $\rightarrow \ell$ j) or a lepton neutrino and a quark (LQ $\rightarrow \nu$ j). The resonance hence is created in that decay channel. For example,

- For a leptoquark of charge $\pm\frac{2}{3}$e, the top quark decays to lepton neutrino and a leptoquark which subsequently decays to a charged lepton and a quark.

---

[4]For detailed changes to the job options to run in MadGraph see A.2

4. Simulation and Analysis

- For a leptoquark of charge $\pm\frac{1}{3}$e, the top quark decays to a charged lepton and a leptoquark which subsequently decays to lepton neutrino and a quark.

In this model, events with leptoquark of charge $\pm\frac{2}{3}$e are generated.

Differential cross sections of various kinematic variables were studied to find the variables that show a difference with respect to the Standard Model. Primary variables of interest are the lepton transverse momentum (p_T), missing transverse energy (E_T^{miss}), transverse mass (m_T) of the Leptoquark decay to a charged lepton and a quark.

4.5.1. Leptoquark mass - 30 GeV

(a) Muon p_T distribution.

(b) Sum of p_T of E_T^{miss} and m_T (μ and E_T^{miss}).

(c) p_T distribution of E_T^{miss}.

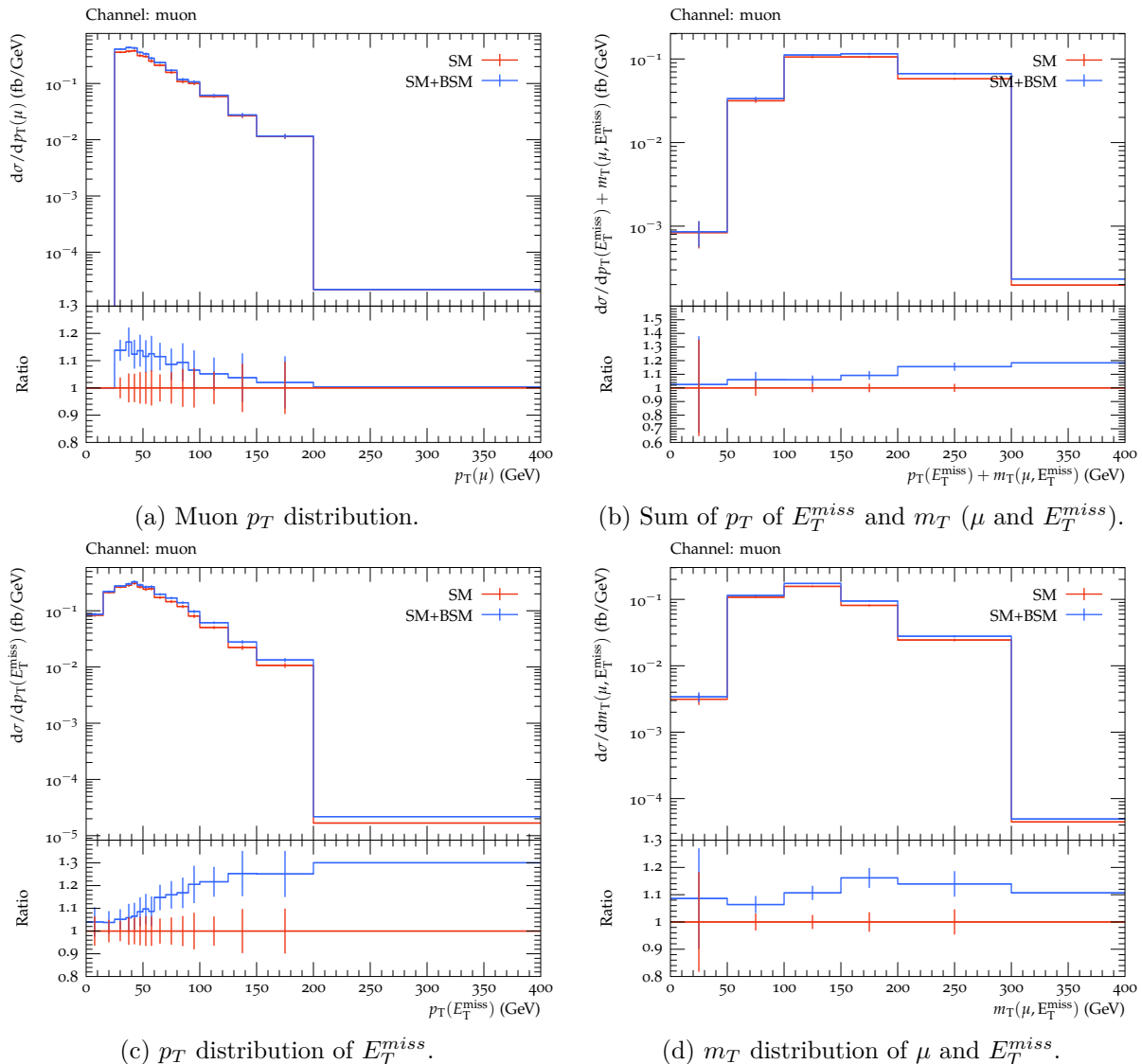(d) m_T distribution of μ and E_T^{miss}.

Figure 4.11.: Distributions of kinematic observables for the leptoquark of mass 30 GeV.

The red line denotes the SM events and the blue line denotes the sum of the SM and the BSM events combined. For a leptoquark of 30 GeV mass, the ratio plot for lepton momentum distributions shows a small BSM shape effect. A higher number of events is observed in the first bins than the last bins in the p_T spectrum because of the lower leptoquark mass, it is energetically more favourable. The muon p_T distribution is shown in figure 4.11(a).

4. Simulation and Analysis

The shape of the sum of the transverse mass of muon and MET, and p_T distribution of E_T^{miss} observable is similar except for the last bin but with no sizeable effect due to the lower leptoquark mass. The sum of the transverse momentum of E_T^{miss} and m_T of muon and E_T^{miss} is shown in figure 4.11(b).

In the p_T spectrum of E_T^{miss} observable, as the resonance is created in the lepton system, a large number of events observed in the last bins opposite the lepton p_T distribution for a low mass leptoquark.

The transverse mass of the lepton and the E_T^{miss} resulting from the decay of a low mass leptoquark is small as can be seen in figure 4.11(d).

4.5.2. Leptoquark mass - 50 GeV

(a) Muon p_T distribution.

(b) Sum of p_T of E_T^{miss} and m_T (μ and E_T^{miss}).

(c) p_T distribution of E_T^{miss}.

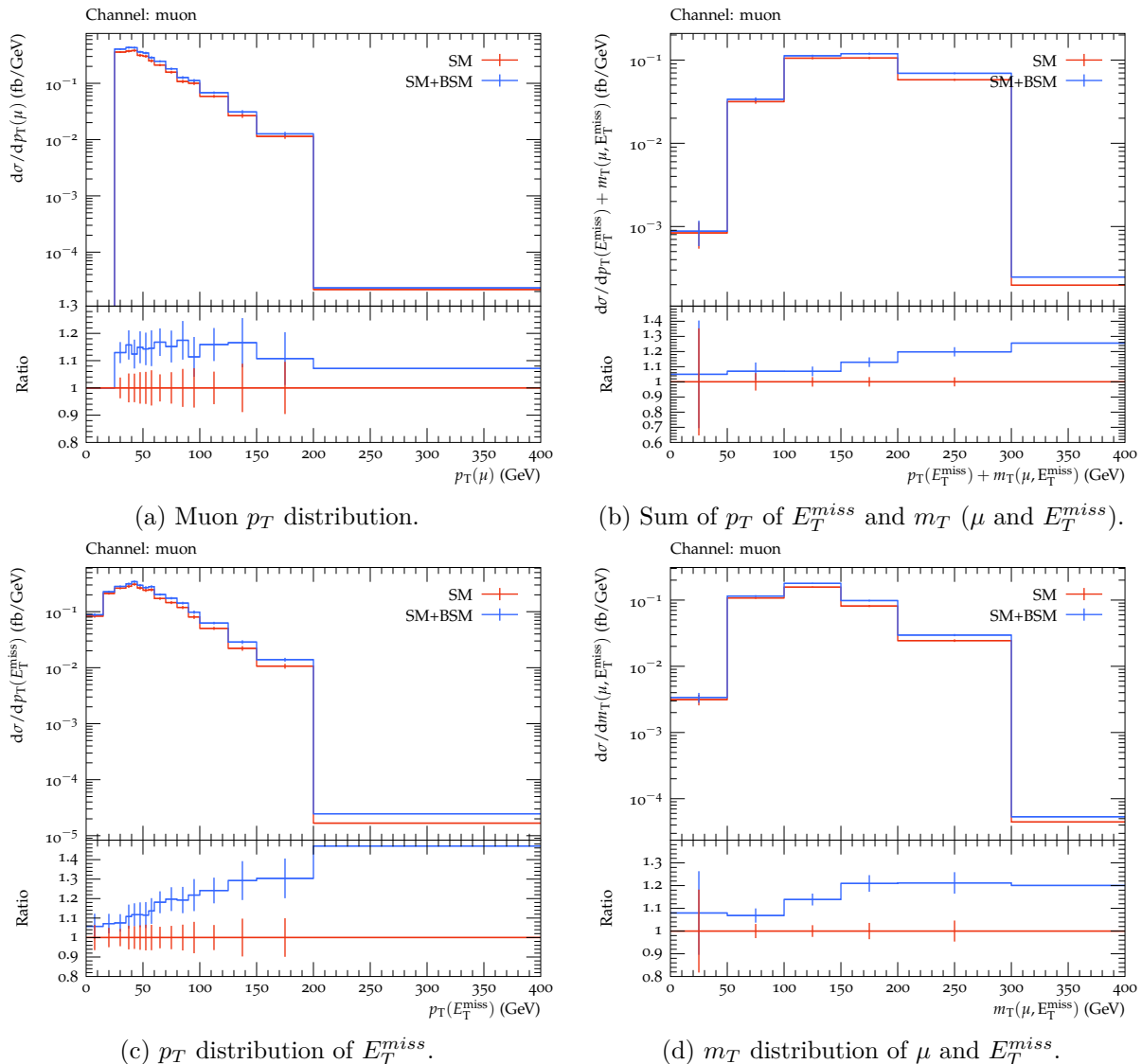(d) m_T distribution of μ and E_T^{miss}.

Figure 4.12.: Distributions of kinematic observables for the leptoquark of mass 50 GeV.

The distributions of the observables for leptoquark mass of 50 GeV are similar to that of leptoquark with a mass of 30 GeV. A large number of events is observed in the first bins in the muon p_T spectrum as it is energetically more favourable for a leptoquark of mass 50 GeV. The muon p_T distribution is shown in figure 4.12(a).

4. Simulation and Analysis

The distribution of the sum of the transverse mass of muon and MET, and p_T distribution of E_T^{miss} observable is shown in figure 4.12(b). As the low mass leptoquark resonance is created in the charged lepton system the shape effect is observed to be small. The transverse momentum of the E_T^{miss} has large shape effects in the last bin as seen in figure 4.12(c). As the top quark decays to a neutrino and a leptoquark (50 GeV), a large number of events is observed with large transverse momentum of missing E_T. The m_T of the lepton and the E_T^{miss} resulting from the decay of low mass leptoquark is small as can be seen in figure 4.12(d).

4.5.3. Leptoquark mass - 150 GeV

(a) Muon p_T distribution.

(b) Sum of p_T of E_T^{miss} and m_T (μ and E_T^{miss}).

(c) p_T distribution of E_T^{miss}.

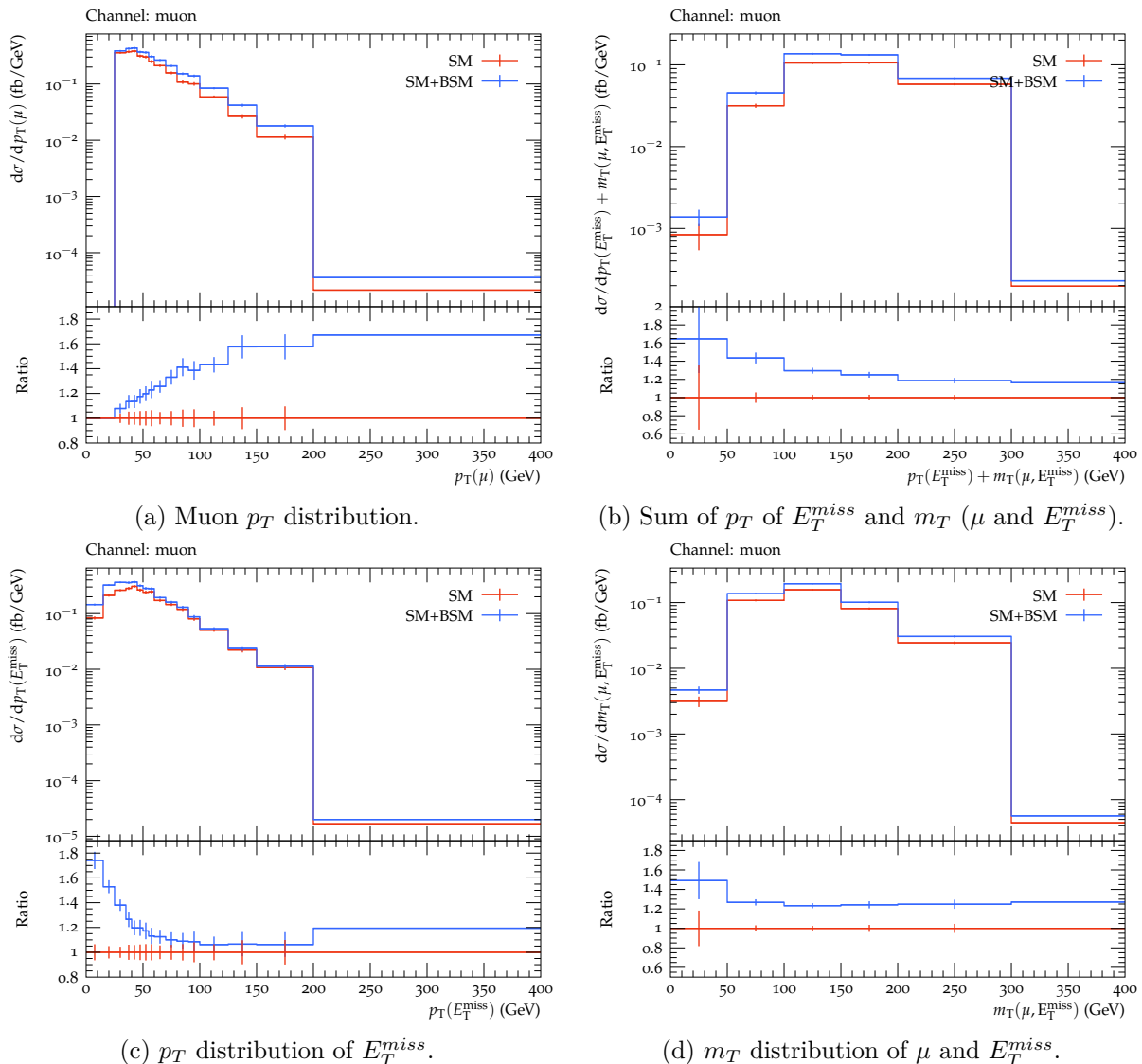(d) m_T distribution of μ and E_T^{miss}.

Figure 4.13.: Distributions of kinematic observables for the leptoquark of mass 150 GeV.

For a leptoquark of mass 150 GeV, the shape of bins in the lepton p_T distribution deviates significantly from the SM. The statistical fluctuations are small and a clear difference is visible. As the leptoquark mass approaches the top mass, lepton p_T in the decay becomes harder. A large number of events with large lepton p_T is observed. The muon p_T distribution is shown in figure 4.13(a).

The shape in the sum of the transverse mass of muon and MET, and the p_T spectrum of E_T^{miss} observable distribution remains as expected. The distribution is shown in figure 4.13(b). For the large mass leptoquark, the transverse momentum of E_T^{miss} now has large

shape effects in the first bin as seen in figure 4.13(c) opposite to the distributions seen in a low mass leptoquark. The m_T distribution is shown in figure 4.21(d).

4.5.4. Leptoquark mass - 170 GeV

(a) Muon p_T distribution.

(b) Sum of p_T of E_T^{miss} and m_T (μ and E_T^{miss}).

(c) p_T distribution of E_T^{miss}.

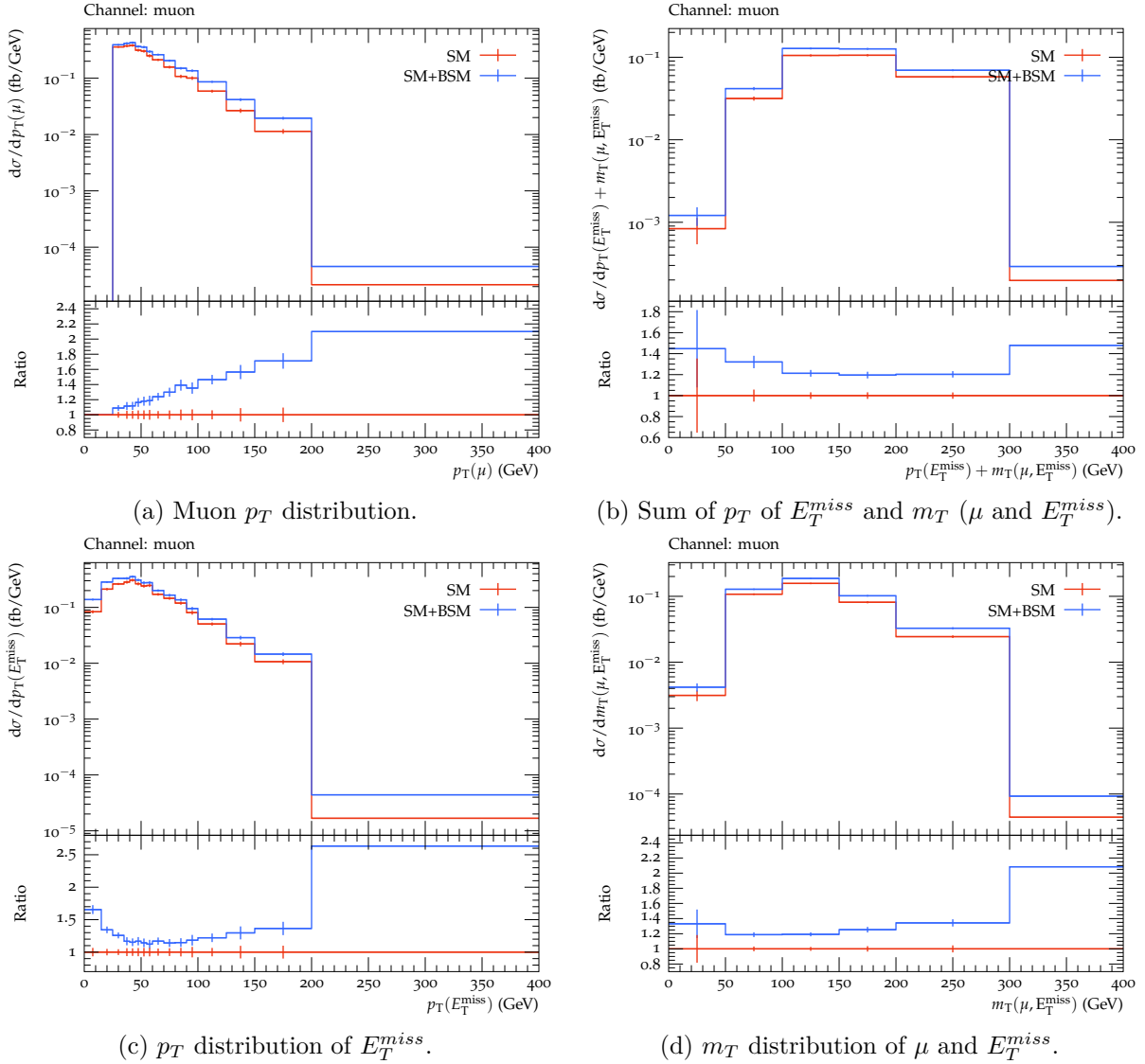(d) m_T distribution of μ and E_T^{miss}.

Figure 4.14.: Distributions of kinematic observables for the leptoquark of mass 170 GeV.

The distributions of the observables for a leptoquark of mass 170 GeV are shown in figure 4.14. A large number of events is observed in the last bins of the muon p_T spectrum as the lepton p_T becomes harder as the leptoquark approaches the top mass. The muon p_T distribution is shown in figure 4.14(a). The shape in the sum of the m_T of muon and MET, and the p_T of E_T^{miss} variable distribution remains as expected. The distribution is shown in figure 4.14(b). The m_T of the lepton and the E_T^{miss} resulting from the decay of low mass leptoquark is small as can be seen in figure 4.14(d).

4.6. The charged Higgs H^+ model

The Higgs boson is a scalar particle of the Standard Model. The charged Higgs boson is a hypothetical particle that is predicted in several extensions of the SM that add a second doublet [59][60] or triplet to its scalar sector [61–64]. There are Higgs models that extend the higgs sector of the SM such as composite Higgs models (CHM)[65], the two-Higgs-doublet model (2HDM) [66], and the three-Higgs-doublet model (3HDM) [67].

Any BSM Higgs extensions must not violate experimental and theoretical constraints such as the

- ρ constraint,

$$\rho = \frac{M_W^2}{M_Z^2 \cos^2\theta_W} = \frac{\Sigma_{i=1}^n [I_i(I_i + 1) - \frac{1}{4}Y_i^2]\nu_i}{\Sigma_{i=1}^n \frac{1}{2}Y_i^2 \nu_i} \approx 1 \tag{4.1}$$

  where M_W is the mass of W boson, M_Z is the mass of Z boson, I is the iso-spin, Y is the hypercharge, and ν is the vacuum expectation value.

- Constraint on the Flavour-changing-neutral-current (FCNC) interactions.

- Unitarity constraint.

As long as these constraints are fulfilled, different Higgs extensions can be foreseen. One of the simplest approaches is the two-Higgs-doublet model, to add an additional complex scalar doublet (Φ_1 and Φ_2).

$$H_1 = \begin{pmatrix} H_1^+ \\ H_1^0 \end{pmatrix} \equiv \frac{\nu_1^* \Phi_1 + \nu_2^* \Phi_2}{\nu} \tag{4.2}$$

$$H_2 = \begin{pmatrix} H_2^+ \\ H_2^0 \end{pmatrix} \equiv \frac{-\nu_2^* \Phi_1 + \nu_1^* \Phi_1}{\nu} \tag{4.3}$$

Two doublets have 8 degrees of freedom, 3 of which give rise to the W and Z boson masses and the other 5 correspond to a total of 5 physical scalars: h (Higgs boson, CP-even scalar[5]), H (CP-even scalar $m_H > m_h$), A (CP-odd pseudoscalar) and charged Higgs ($H^\pm$). Production and decay of the charged Higgs depend on its mass, mixing angle (α), and the ratio between the vacuum expectation values of the two complex doublets $\tan\beta$.

---

[5]CP - Charge Parity

Depending on the type of fermions coupling to the doublets, 2HDM is again classified into 4 types as shown in table 4.1.

Type I	The charged fermions only couple to Φ_2
Type II	Leptons and up-type quarks couple to Φ_1, down-type couple to Φ_2
Type X/Y	Quarks and leptons couple to opposite Φ
Type III	FCNCs at tree level

Table 4.1.: Classification of types in the two-Higgs-doublet model.

Recent searches for charged Higgs bosons lighter or heavier than the top quark, including the intermediate region, were performed by ATLAS using 36.1 fb^{-1} of data collected at $\sqrt{s} = 13$ TeV in 2015 and 2016, in the decay $\tau\nu$ mode [68]. Current mass limits for $m_{H^\pm} < m_{top}$ is m > 155 GeV at 95% CL and for $m_{H^\pm} > m_{top}$ is m > 181 GeV at 95% CL ($\tan\beta = 10$) [16].
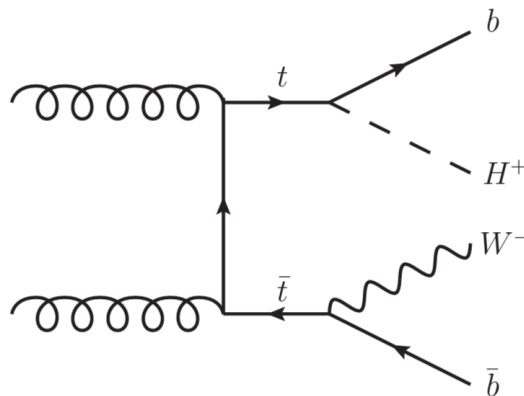

Figure 4.15.: Feynman diagram representing a charged Higgs boson interaction in a top quark decay.

In this analysis, the focus is placed on the charged Higgs from type II 2HDM to muon and its neutrino. Charged Higgs production from $t\bar{t}$ decay in the model used in this analysis is shown in figure 4.15, where one (anti) top quark decays via BSM to a (conjugate[6]) charged Higgs and the other top quark decays via the SM to a W boson. Subsequently, the Charged Higgs decays to a charged lepton and a neutrino. Since the study is focused on

---

[6]conjugate charged Higgs refers to a charged Higgs with an opposite electric charge

the muon channel, only the charged Higgs coupling to a muon and its neutrino is turned on. Hence, in this model, the charged Higgs decays to the second generation lepton pair only.
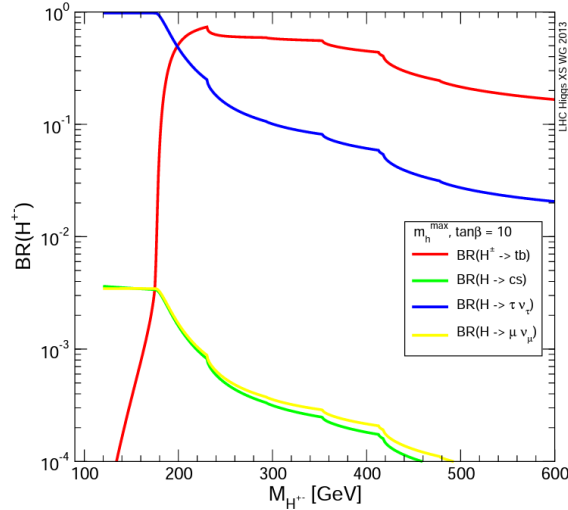

Figure 4.16.: Branching fractions of the charged Higgs boson as a function of the mass of charged Higgs boson ($m_{H^\pm}$), for $\tan\beta = 10$ [69].

On-shell $t\bar{t}$ events are generated by the MadGraph5_aMC@NLO [7] [43] generator within the Athena framework and interfaced with Pythia 8 (v.245) [53] to simulate parton shower. EvtGen (v.1.7) was used to simulate (b-)hadron decays. The charged Higgs boson mass ($m_{H^\pm}$) range considered for the study is 10 GeV to 160 GeV below the mass of the top quark. As the mass of the charged Higgs changes, the branching ratio of the charged Higgs to the fermion changes. Branching fractions of the charged Higgs as a function of $m_{H^\pm}$ are shown in figure 4.16. In the studied $m_{H^\pm}$ range (60 - 160 GeV), the branching fraction of the charged Higgs to fermions is almost constant (0.0035104). The observed cross section exhibits an exponential decrease as the charged Higgs boson mass increases as seen in figure 4.17.

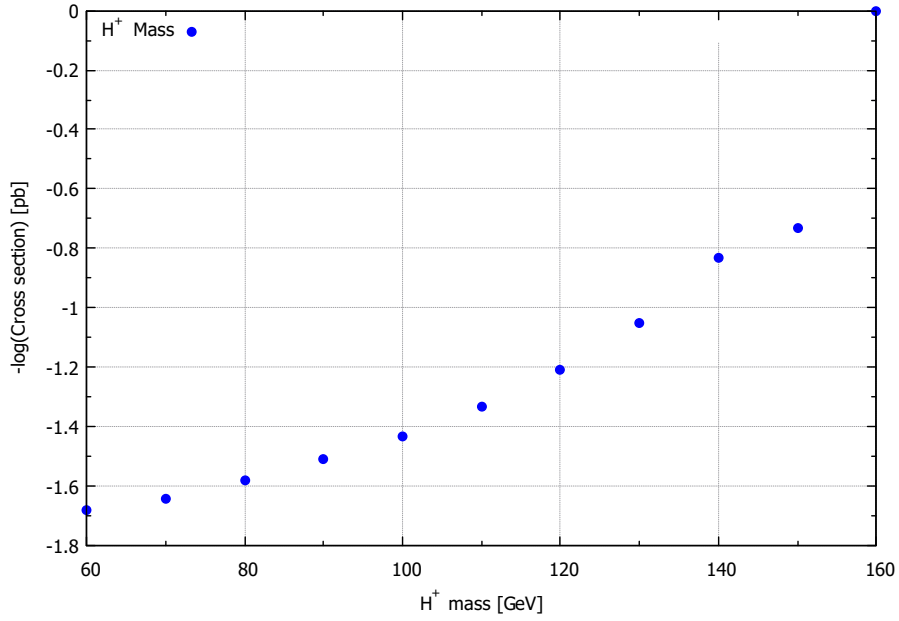[7]For detailed changes to the job options to run in MadGraph see A.3

Figure 4.17.: Negative logarithmic scale of Cross section as a function of the charged Higgs boson mass.

Similar to the previous two models (W' and Leptoquark), the lepton transverse momentum (p_T), missing transverse energy (E_T^{miss}), and transverse mass (m_T) observables are studied in the charged Higgs model analysis.

4.6.1. H^+ mass - 60 GeV

(a) Muon p_T distribution.

(b) Sum of p_T of E_T^{miss} and m_T (μ and E_T^{miss}).

(c) p_T distribution of E_T^{miss}.
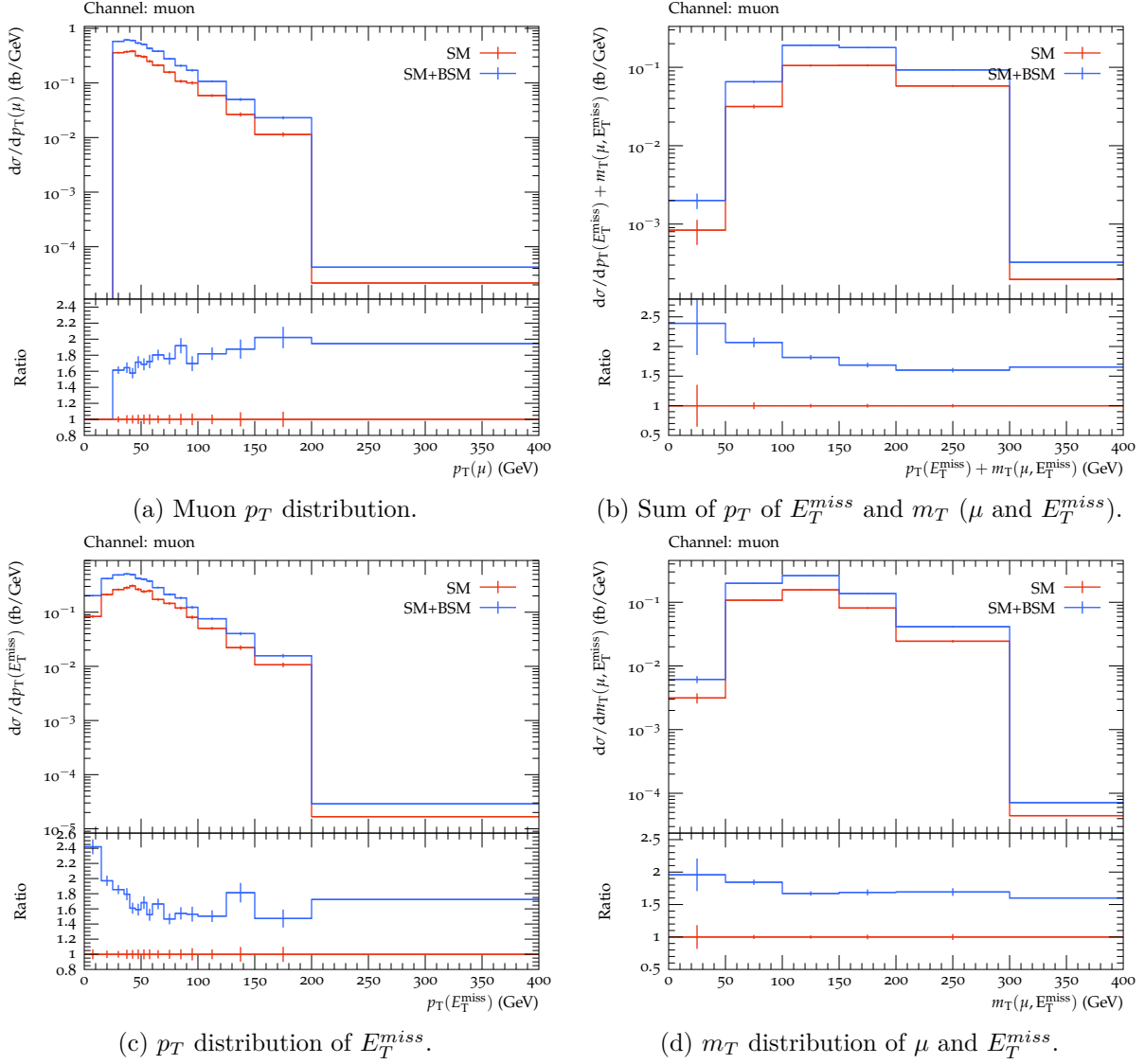
(d) m_T distribution of μ and E_T^{miss}.

Figure 4.18.: Distributions of kinematic observables for the charged Higgs boson of mass 60 GeV.

The red line denotes the SM events and the blue line denotes both the SM and the BSM events combined. The SM events are centred at 1 in the ratio to compare the effects of the BSM against the SM. Considering the statistical fluctuations, small BSM shape effects are observed in the lepton momentum distributions for the charged Higgs boson of mass 60 GeV. The muon P_T distribution is shown in figure 4.18(a).

Looking at the shape of the sum of the transverse mass of muon and MET, and the p_T spectrum of E_T^{miss} observable is similar, with no sizeable effect due to the lower charged Higgs boson mass. The sum of the lepton p_T of E_T^{miss} and transverse mass of muon and E_T^{miss} is shown in figure 4.18(b).

In the spectrum of the p_T of E_T^{miss} for the charged Higgs boson a large number of events are observed in the first bins of the p_T of E_T^{miss} distribution as expected for a low mass charged Higgs boson. The p_T distribution for E_T^{miss} is shown in figure 4.18(c).

The m_T shape effects of the lepton and the E_T^{miss} resulting from the decay of the low mass charged Higgs boson are small as can be seen in figure 4.18(b).

4.6.2. H^+ mass - 80 GeV

(a) Muon p_T distribution.

(b) Sum of p_T of E_T^{miss} and m_T (μ and E_T^{miss}).

(c) p_T distribution of E_T^{miss}.
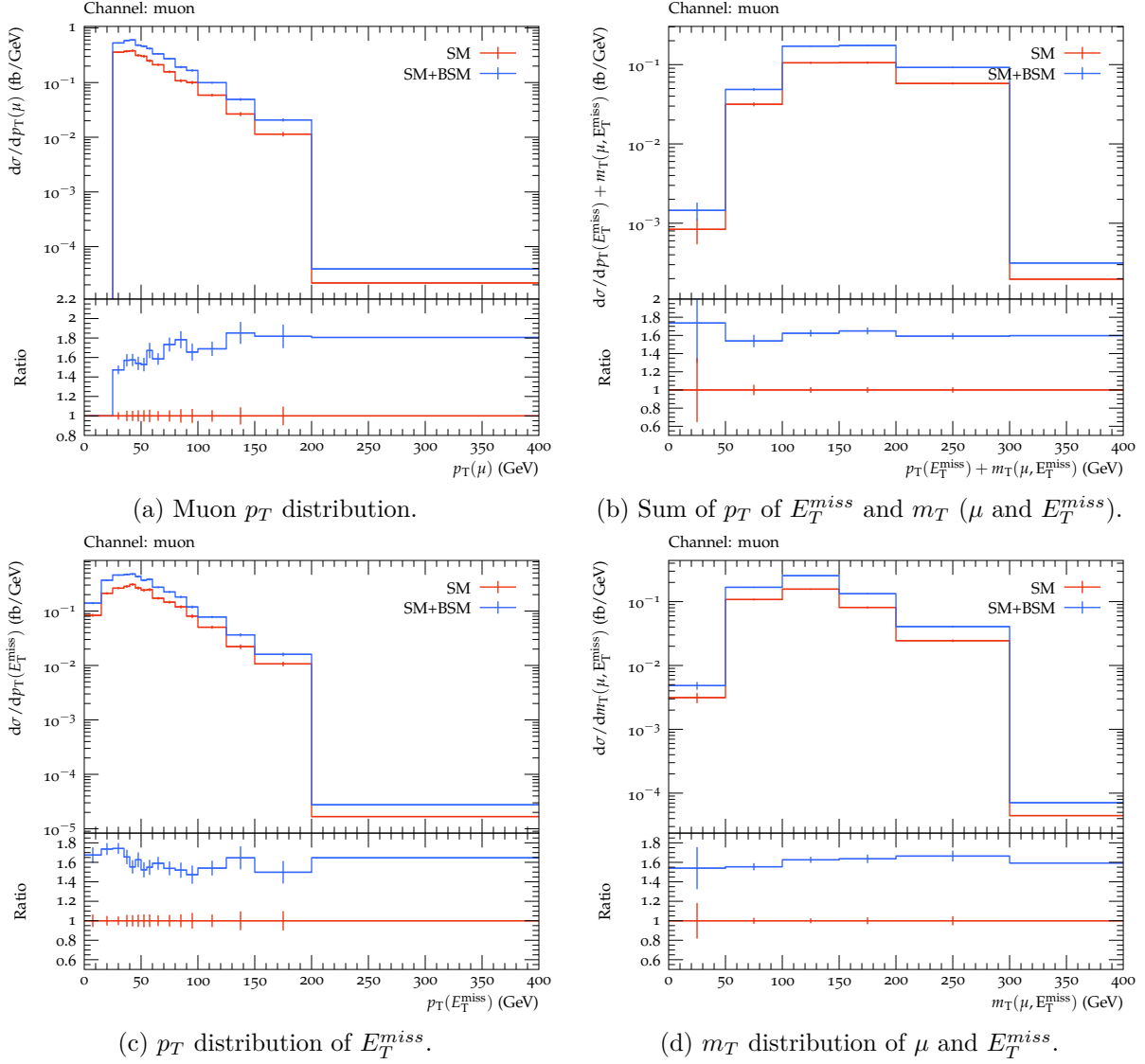
(d) m_T distribution of μ and E_T^{miss}.

Figure 4.19.: Distributions of kinematic observables for the charged Higgs boson of mass 80 GeV.

There is no large difference between the distributions of the observables for charged Higgs mass of 80 GeV to that of charged Higgs with a mass of 60 GeV. A large number of events are observed in the first bins in the muon p_T spectrum as it is energetically more favourable for a charged Higgs of mass 80 GeV. The muon p_T distribution is shown in figure 4.19(a). Because of the low mass boson, events with softer lepton p_T are observed in the last bins of the distribution.

The sum of the m_T of muon and MET, and the p_T spectrum of E_T^{miss} observable is shown in figure 4.19(b). p_T distribution for E_T^{miss} is shown in figure 4.19(c). The m_T spectrum of the lepton and the E_T^{miss} resulting from the decay of a low mass charged Higgs boson is shown in figure 4.19(b).

4.6.3. H^+ mass - 120 GeV

(a) Muon p_T distribution.

(b) Sum of p_T of E_T^{miss} and m_T (μ and E_T^{miss}).

(c) p_T distribution of E_T^{miss}.

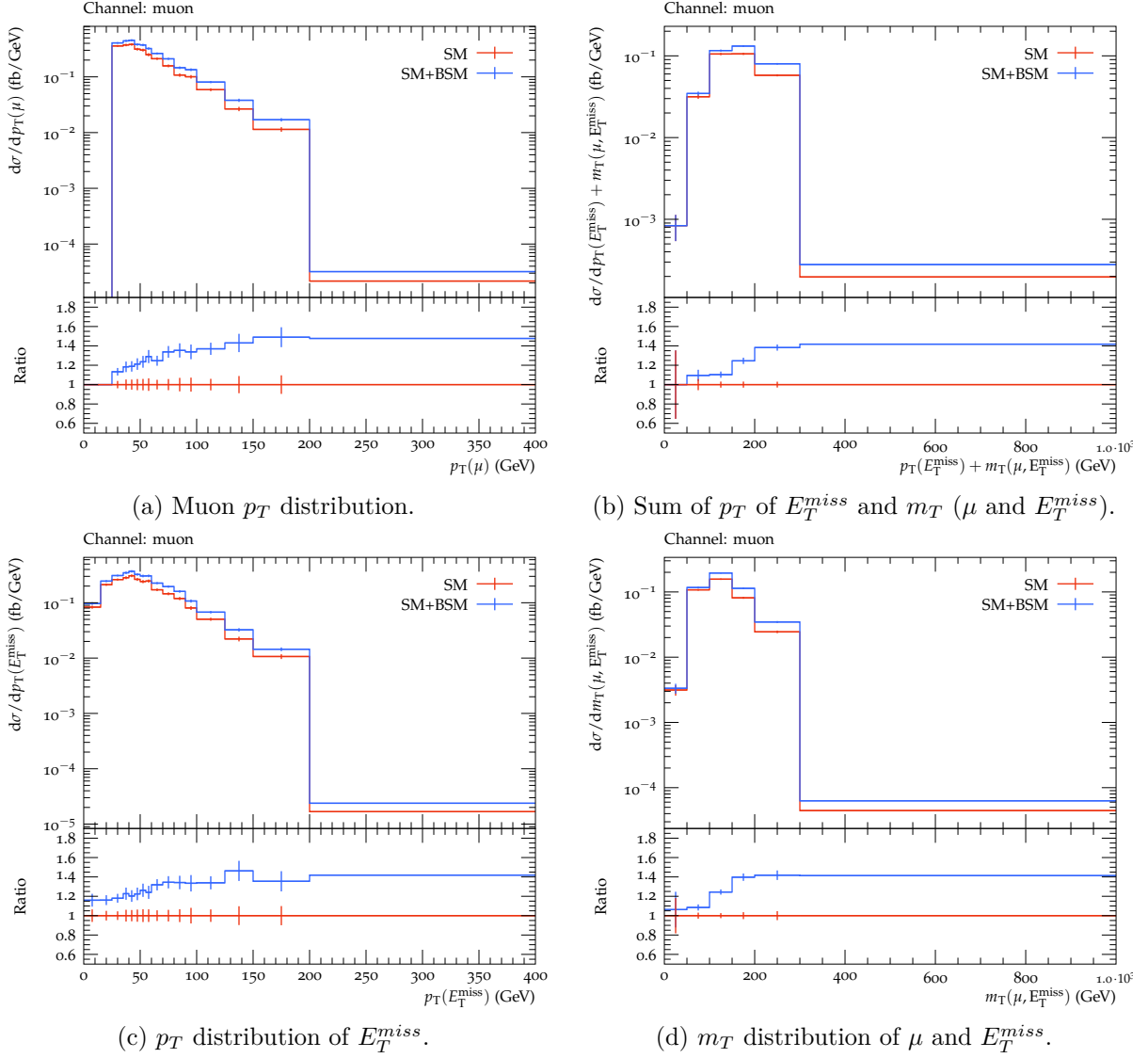(d) m_T distribution of μ and E_T^{miss}.

Figure 4.20.: Distributions of kinematic observables for the charged Higgs boson of mass 120 GeV.

A large number of events is observed in the last bins of the distributions for heavy charged Higgs boson compared to the previous two cases. As the charged Higgs boson mass increases, events with harder lepton p_T in the decay are observed. A significant

shape-shift is observed in the last bins compared to the low mass charged Higgs boson. The muon p_T distribution is shown in figure 4.20(a).

A shift in the number of events from the first bin to the last bin is observed in the kinematic distributions as the charged Higgs boson mass increased from 80 GeV to 120 GeV as expected. Kinematic variable distributions for charged Higgs boson of mass 120 GeV are shown in figures 4.20(c)-4.20(d).
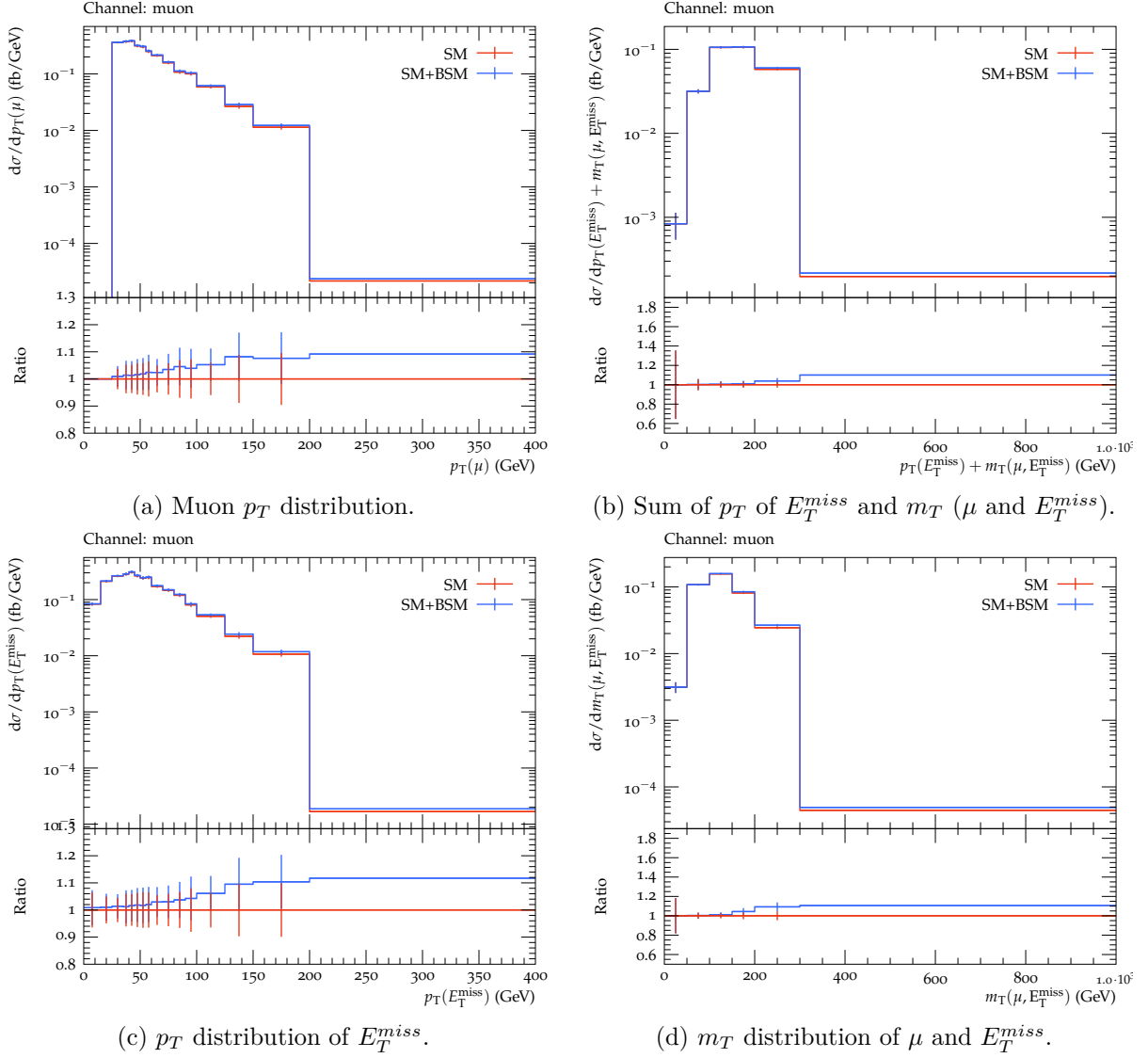
4.6.4. H^+ mass - 150 GeV

(a) Muon p_T distribution.

(b) Sum of p_T of E_T^{miss} and m_T (μ and E_T^{miss}).

(c) p_T distribution of E_T^{miss}.

(d) m_T distribution of μ and E_T^{miss}.

Figure 4.21.: Distributions of kinematic observables for the charged Higgs boson of mass 150 GeV.

As the charged Higgs boson approached the top quark mass, the cross section is reduced for this on-shell process. The distribution still exhibits similar shape effects as shown in the distribution for the muon p_T distribution for the charged Higgs boson mass of 120 GeV (see figure 4.20(a)). Events are observed in large numbers in the last bins of the p_T distribution. The muon p_T distribution for the charged Higgs boson of mass 150 GeV is shown in figure 4.21(a).

The sum of the lepton p_T of MET and m_T of muon and E_T^{miss} is shown in figure 4.21(b).

The p_T distribution for E_T^{miss} is shown in figure 4.21(c). The transverse mass spectrum of the lepton and the E_T^{miss} resulting from the decay of low mass charged Higgs boson is shown in figure 4.21(b). All these distributions show a large number of events in the last bins compared to their first bins.

These three truth-level observables from the three BSM models (W', Leptoquark, and charged Higgs) are folded to reco level distributions via a folding method[8] and compared to the Standard Model Monte Carlo distributions. The SM events are generated using Powheg+Pythia8 and using EvtGen for b-hadron decays.

---

[8]See chapter 4.3

5. Conclusion and Outlook

The $t\bar{t}$ decay to single lepton plus jets channel provides a good opportunity to probe the lepton universality. As the top quark decays to the single charged lepton, it provides a better signal compared to other decay channels to have a deeper insight into the lepton universality. Hence the single lepton channel of the top quark pair decay is studied. In this analysis, low mass particles inter-mediating the top quark decay are studied as the current searches are more focused on the phase space and kinematics of high energetic particles of TeV range. Low energetic BSM particles are excluded based on old searches and with the current power of detectors, it is useful to revisit the excluded low energetic BSM particles.

Hence in this analysis, events in the simplified BSM models (W', Leptoquark, and charged Higgs) are generated and the kinematic variables that display distinct shape effects from the SM variables are studied. Three observables; lepton transverse momentum, MET, and transverse mass are compared to the Standard Model Monte Carlo via folding and the limits on the stat-only fit of signal strength (μ) and cross section are obtained.
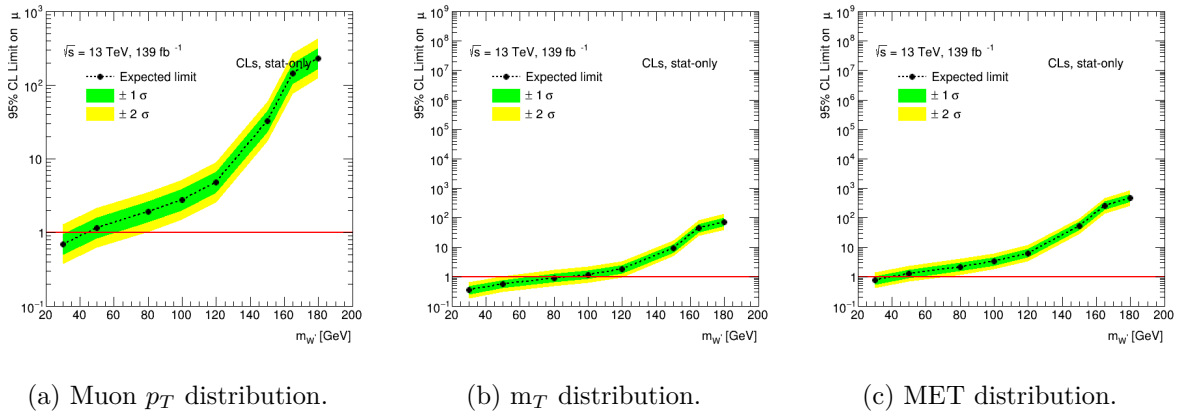

(a) Muon p_T distribution.   (b) m$_T$ distribution.   (c) MET distribution.

Figure 5.1.: stat-only fit limits on the signal strength (μ) for the W' model as a function of m$_{W'}$ [70]. The red line centred at 1 shows the μ in the SM. The green band around the expected limit denotes the 1σ region and the yellow band denotes the 2σ region.

Stat-only fit limits at 95% CL (confidence limit) on the μ for the W' model as a function

5. Conclusion and Outlook

of the W' mass is shown in figure 5.1. The ratio between the cross section of the BSM and the SM signal process is represented by μ. As observed in figures 5.1(a)-5.1(c), the sensitivity is reduced as the mass of W' approaches the top quark mass because of the smaller cross section. In the stat-only fit, very small masses are expected to be excluded as they already have low $\mu < 1$.

(a) Muon p_T distribution. (b) m_T distribution. (c) MET distribution.
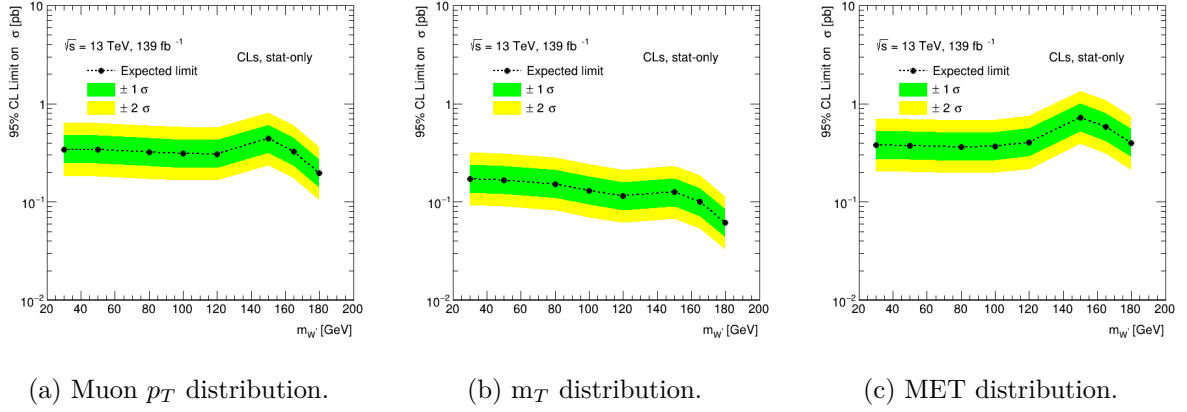
Figure 5.2.: stat-only fit limits on the cross section for the W' model as a function of $m_{W'}$ [70]. The green band around the expected limit denotes the 1σ region and the yellow band denotes the 2σ region.

Stat-only fit limits at 95% CL on the cross section for the W' model as a function of the W' mass is shown in figure 5.2. The plots show the sensitivity of the cross sections obtained from the stat-only fit of the W' model. The sensitivity of the cross section obtained for this W' model is in the order of 0.1 - 1 pb across the three folded observables.

(a) Muon p_T distribution.

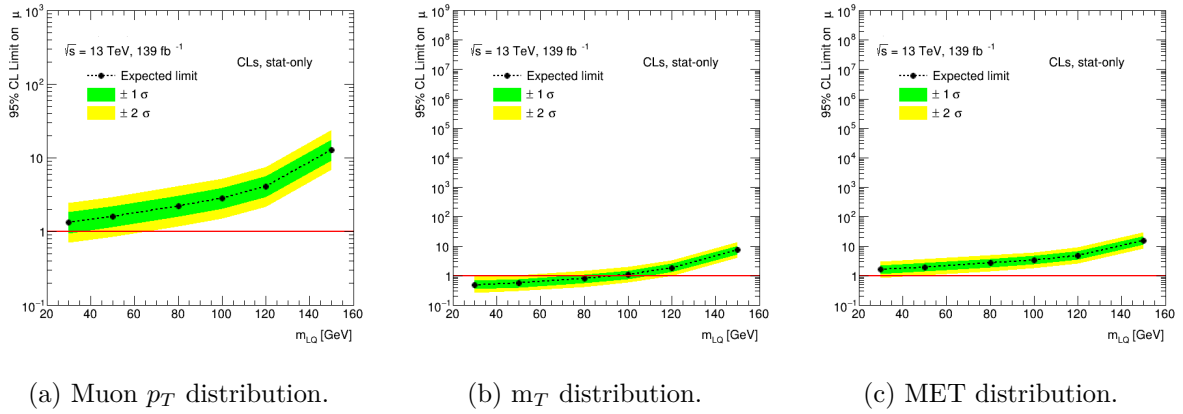(b) m_T distribution.

(c) MET distribution.

Figure 5.3.: stat-only fit limits on the μ for the Leptoquark model as a function of m_{LQ} [70]. The red line centred at 1 shows the μ in the SM. The green band around the expected limit denotes the 1σ region and the yellow band denotes the 2σ region.

Figure 5.3 shows the stat-only fit limits at 95% CL on the signal strength for the Leptoquark model as a function of the leptoquark mass. The sensitivity is reduced as the mass of the leptoquark approaches the top quark mass, the cross section falls exponentially.

(a) Muon p_T distribution.
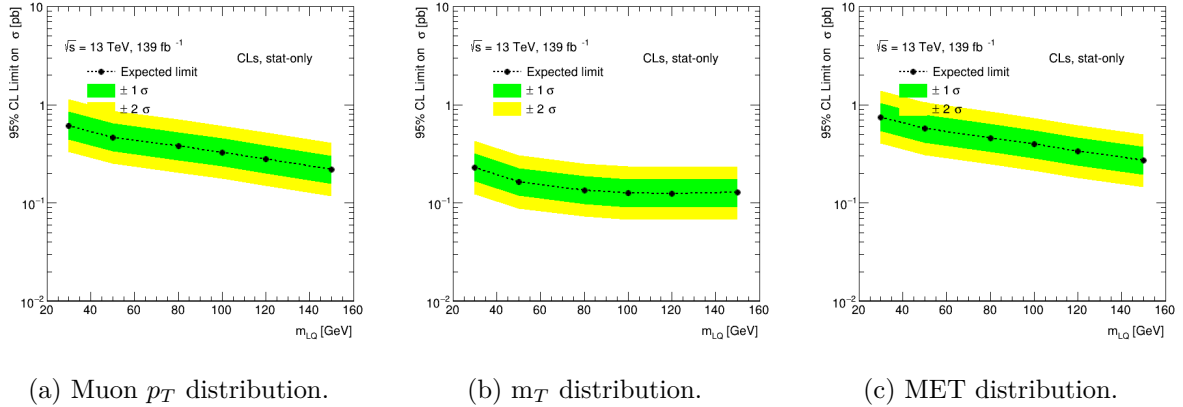
(b) m_T distribution.

(c) MET distribution.

Figure 5.4.: stat-only fit limits on the cross section for the Leptoquark model as a function of m_{LQ} [70]. The green band around the expected limit denotes the 1σ region and the yellow band denotes the 2σ region.

Stat-only fit limits at 95% CL on the cross section for the Leptoquark model as a function of the Leptoquark mass is shown in figure 5.4. The plots show the sensitivity of the cross sections obtained from the stat-only fit of the Leptoquark model. The sensitivity of the cross section obtained for this leptoquark model is also in the order of 0.1 - 1 pb across the three folded observables.

Stat-only fit limits at 95% CL (confidence limit) on the μ for the charged Higgs model
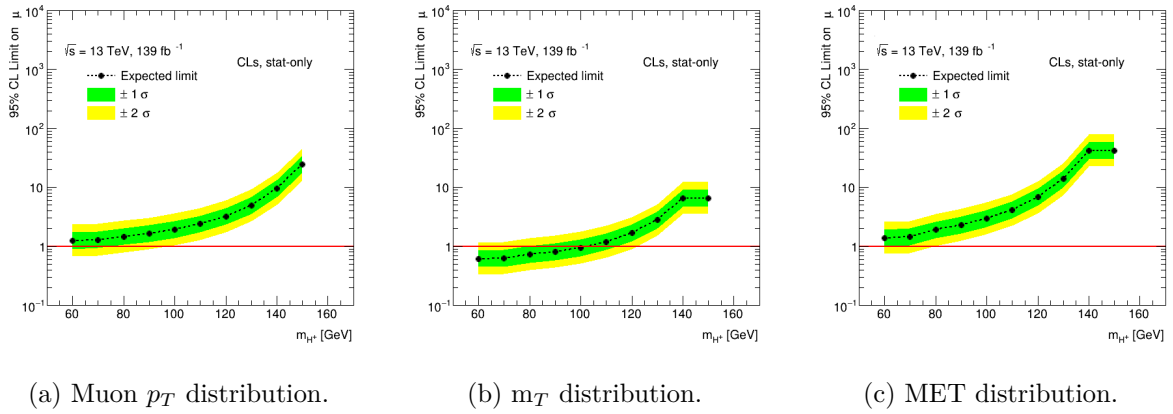
5. Conclusion and Outlook

(a) Muon p_T distribution.
(b) m_T distribution.
(c) MET distribution.

Figure 5.5.: stat-only fit limits on the μ for the charged Higgs model as a function of m_{H+} [70]. The red line centred at 1 shows the signal strength in the SM. The green band around the expected limit denotes the 1σ region and the yellow band denotes the 2σ region.

as a function of the charged Higgs mass is shown in figure 5.5. The sensitivity is reduced as the mass of charged Higgs approaches the top quark mass because of the smaller cross section at higher charged Higgs mass.
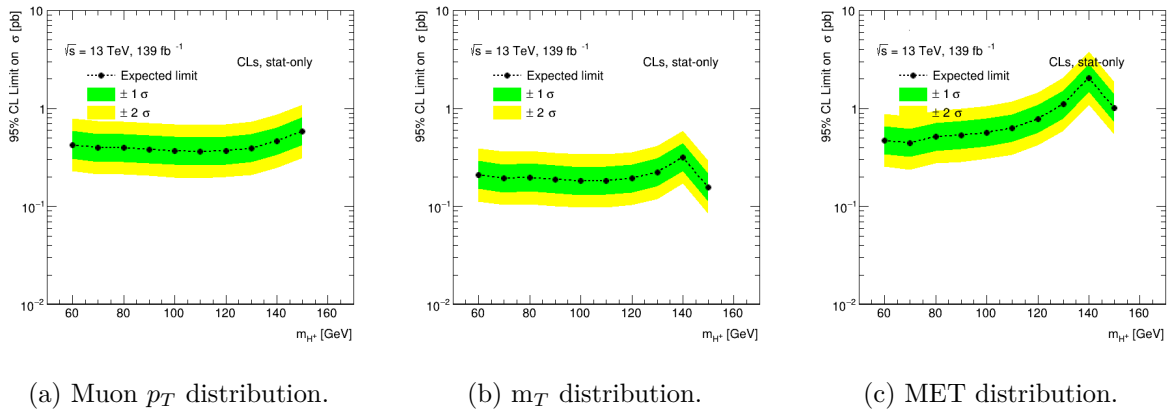

(a) Muon p_T distribution.
(b) m_T distribution.
(c) MET distribution.

Figure 5.6.: stat-only fit limits on the cross section for the charged Higgs model as a function of m_{H+} [70]. The green band around the expected limit denotes the 1σ region and the yellow band denotes the 2σ region.

Stat-only fit limits at 95% CL on the cross section for the charged Higgs model as a function of the charged Higgs mass are shown in figure 5.6. The sensitivity of the cross section obtained for this leptoquark model is in the order of 0.1 - 1 pb. The kink at the charged Higgs mass of 140 GeV can be explained due to the lower statistics of the observables; transverse mass and MET distributions in the charged Higgs model.

This concludes my thesis on the Monte Carlo simulation study of the BSM models in the single lepton channel (muon channel) decay of the top quark pair with $\sqrt{s} = 13$ TeV and an integrated luminosity of 139 fb^{-1} to investigate the solutions for a potential lepton universality violation. This thesis dealt with the Monte Carlo simulation study of the BSM processes and selection of the observables with distinct shape effects from the SM observables and obtaining the limits on the μ and cross section on the stat-only fit. Even though, from the stat-only fit on the BSM models, lower masses are expected to be excluded. They are dominated by the systematic effects which are not studied in this analysis. This analysis can be further developed by including the effect of systematics. Exclusion limits on the BSM models can then be obtained with the study of full systematics and comparing to the actual data.

A. Modifications in MadGraph

MadGraph is used within the Athena framework. Modifications are written in the python script that generates the required process. The changes are applied to the parameter card and run card.

A.1. The W' model

Processes are generated with the number of vertices QCD = 2, WP(W') = 2, QED = 2. The exact changes are given below:

- The branching Ratio of W' to leptons is assumed to be constant for all W' masses.

- For the W' model, in parameter card New Physics block:

PDG ID	Coupling	comments
7	0.1	W' coupling to left-handed quarks
8	0.1	W' coupling to right-handed quarks
9	0.0	W' coupling to left-handed leptons of first generation
10	0.0	W' coupling to right-handed leptons of first generation
11	0.1	W' coupling to left-handed leptons of second generation
12	0.1	W' coupling to right-handed leptons of second generation
13	0.0	W' coupling to left-handed leptons of third generation
14	0.0	W' coupling to right-handed leptons of third generation

- For the W' model, in parameter card Mass block. Mass is updated for every new event generation for a different mass:

A. Modifications in MadGraph

PDG ID	Mass (GeV)	comments
34	100.0	W' mass

- For the W' model, in run card:

Settings	Value
lhe version	3.0
pdlabel	lhapdf
lhaid	260000
number of events	1000000
bwcutoff (Breit-wigner)	150.0

A.2. The Leptoquark model

For leptoquark events, processes are generated with the number of vertices QCD = 2 LQ(Leptoquark) = 2 QED = 2. The exact changes are given below:

- The branching Ratio of leptoquark to leptons is assumed to be constant for all W' masses.

- For the leptoquark model, in parameter card New Physics block:

PDG ID	Coupling	comments
15	0.1	LQ coupling to left-handed quarks of first generation
16	0.1	LQ coupling to right-handed quarks of first generation
17	0.1	LQ coupling to left-handed quarks of second generation
18	0.1	LQ coupling to right-handed quarks of second generation
19	0.1	LQ coupling to left-handed quarks of third generation
20	0.1	LQ coupling to right-handed quarks of third generation
21	0.0	LQ coupling to left-handed leptons of first generation
22	0.0	LQ coupling to right-handed leptons of first generation
23	0.1	LQ coupling to left-handed leptons of second generation
24	0.1	LQ coupling to right-handed leptons of second generation
25	0.0	LQ coupling to left-handed leptons of third generation
26	0.0	LQ coupling to right-handed leptons of third generation

- For the leptoquark model, in parameter card Mass block. Mass is updated for every new event generation for a different mass:

PDG ID	Mass (GeV)	comments
42	30.0	Leptoquark mass

A. Modifications in MadGraph

- For leptoquark model, in run card:

Settings	Value
lhe version	3.0
pdlabel	lhapdf
lhaid	260000
number of events	1000000
bwcutoff (Breit-wigner)	150.0

A.3. The charged Higgs H^+ model

- For charged Higgs boson model, the events are generated using 2HDM model.

- Unlike the other two models, the coupling constant is not an arbitrary constant and cannot be changed manually.

- The branching fractions of the charged Higgs boson to fermions is almost constant throughout the mass range under study.

- For the charged Higgs boson model, in parameter card Mass block. Mass is updated for every new event generation for a different mass:

PDG ID	Mass (GeV)	comments
37	60.0	charged Higgs mass

- For the charged Higgs boson model, in run card:

Settings	Value
lhe version	3.0
pdlabel	lhapdf
lhaid	262400
number of events	1000000
bwcutoff (Breit-wigner)	15.0

- Charged Higgs decay to the muon and its neutrino is turned on manually in the job.

B. Plots

Evolution of the $\Delta\phi$ distribution is shown in figure B.1 as a function of the W' mass in the range between 10 GeV and 165 GeV. A shift of the shape is observed from the first bin to the last bin as the mass of the W' boson is increased.
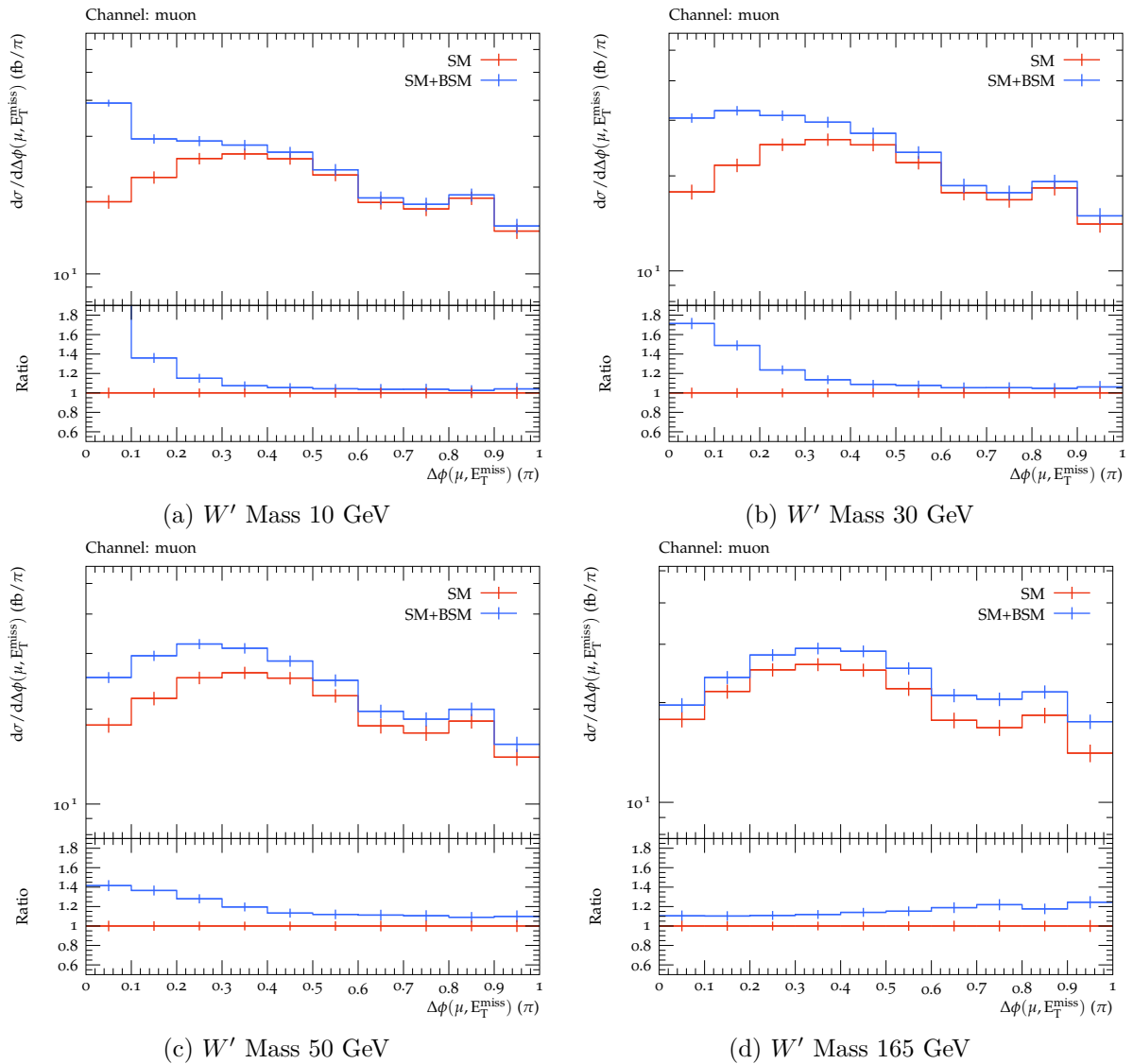

(a) W' Mass 10 GeV

(b) W' Mass 30 GeV

(c) W' Mass 50 GeV

(d) W' Mass 165 GeV

Figure B.1.: Evolution of the $\Delta\phi$ distribution as a function of the W' mass range between 10 GeV and 165 GeV.

Bibliography

[1] A. Salam and J. C. Ward, *Electromagnetic and weak interactions*, Phys. Lett. **13** (1964) 168.

[2] S. L. Glashow, *Partial-symmetries of weak interactions*, Nucl. Phys. **22** (1961) 579.

[3] S. Weinberg, *A Model of Leptons*, Phys. Rev. Lett. **19** (1967) 1264.

[4] D. J. Gross and F. Wilczek, *Ultraviolet Behavior of Non-Abelian Gauge Theories*, Phys. Rev. Lett. **30** (1973) 1343.

[5] H. D. Politzer, *Reliable Perturbative Results for Strong Interactions?*, Phys. Rev. Lett. **30** (1973) 1346.

[6] G. 't Hooft and M. Veltman, *Regularization and renormalization of gauge fields*, Nucl. Phys. B **44** (1972) 189.

[7] G. 't Hooft and M. Veltman, *Combinatorics of gauge fields*, Nucl. Phys. B **50** (1972) 318.

[8] The ATLAS Collaboration, *Observation of a new particle in the search for the Standard Model Higgs boson with the ATLAS detector at the LHC*, Phys. Rev. Lett. B **716** (2012) 1.

[9] The CMS Collaboration, *Observation of a new boson at a mass of 125 GeV with the CMS experiment at the LHC*, Phys. Rev. Lett. B **716** (2012) 30.

[10] J. R. Ellis, *Limits of the Standard Model*, tech. rep., CERN, Geneva, Nov, 2002.

[11] SNO Collaboration, Q. R. Ahmad et al., *Direct Evidence for Neutrino Flavor Transformation from Neutral-Current Interactions in the Sudbury Neutrino Observatory*, Phys. Rev. Lett. **89** (2002) 011301.

[12] A. Arbey and F. Mahmoudi, *Dark matter and the early Universe: A review*, Prog. Part. Nucl. Phys. (2021).

Bibliography

[13] The LHCb Collaboration, *Test of lepton universality in beauty-quark decays*, Nat. Phys. **18** (2022) 277.

[14] The BELLE Collaboration, *Test of lepton flavor universality and search for lepton flavor violation in B → kll decays*, JHEP **2021** (2021).

[15] P. A. M. Dirac, *The Quantum Theory of the Electron*, Proc. R. Soc. A **117** (1928) 610.

[16] Particle Data Group Collaboration, R. L. Workman and Others, *Review of Particle Physics*, PTEP **2022** (2022) 083C01.

[17] C. S. Wu et al., *Experimental Test of Parity Conservation in Beta Decay*, Phys. Rev. **105** (1957) 1413.

[18] M. Goldhaber, L. Grodzins and A. W. Sunyar, *Helicity of Neutrinos*, Phys. Rev. **109** (1958) 1015.

[19] M. Kobayashi and T. Maskawa, *CP-Violation in the Renormalizable Theory of Weak Interaction*, Prog. Theor. Phys. **49** (1973) 652.

[20] N. Cabibbo, *Unitary Symmetry and Leptonic Decays*, Phys. Rev. Lett. **10** (1963) 531.

[21] A. Djouadi, *The anatomy of electroweak symmetry breaking*, Phys. Rep. **457** (2008) 1.

[22] The ATLAS Collaboration, *Measurement of the Higgs boson mass in the $H{\rightarrow}ZZ^* {\rightarrow}4l$ and $H{\rightarrow}\gamma\gamma$ channels with $\sqrt{s}$ = 13 TeV pp collisions using the ATLAS detector*, Phys. Lett. B **784** (2018) 345.

[23] The CMS Collaboration, *A measurement of the Higgs boson mass in the diphoton decay channel*, Phys. Lett. B **805** (2020) 135425.

[24] The ATLAS Collaboration, *Evidence for the spin-0 nature of the Higgs boson using ATLAS data*, Phys. Rev. Lett. B **726** (2013) 120.

[25] The CMS Collaboration, *Study of the Mass and Spin-Parity of the Higgs Boson Candidate via Its Decays to Z Boson Pairs*, Phys. Rev. Lett. **110** (2013) 081803.

[26] The CDF Collaboration, *Observation of Top Quark Production in $\overline{p}p$ Collisions with the Collider Detector at Fermilab*, Phys. Rev. Lett. **74** (1995) 2626.

[27] The D∅ Collaboration, *Observation of the Top Quark*, Phys. Rev. Lett. **74** (1995) 2632.

[28] M. Kobayashi and T. Maskawa, *CP-Violation in the Renormalizable Theory of Weak Interaction*, Prog. Theor. Phys. **49** (1973) 652.

[29] T. Song and H. Berrehrah, *Hadronization time of heavy quarks in nuclear matter*, Phys. Rev. C **94** (2016) 034901.

[30] The ATLAS Collaboration, *Test of the universality of τ and μ lepton couplings in W-boson decays with the ATLAS detector*, Nat. Phys. **17** (2020) 813.

[31] I. Dorvsner et al., *Physics of leptoquarks in precision experiments and at particle colliders*, Phys. Rep. **641** (2016) 1.

[32] The ATLAS Collaboration, *The ATLAS Experiment at the CERN Large Hadron Collider*, JINST **3** (2008) S08003.

[33] L. Evans and P. Bryant, *LHC Machine*, JINST **3** (2008) S08001.

[34] The ALICE Collaboration, *The ALICE experiment at the CERN LHC*, JINST **3** (2008) S08002.

[35] The LHCb Collaboration, *The LHCb Detector at the LHC*, JINST **3** (2008) S08005.

[36] The CMS Collaboration, *The CMS experiment at the CERN LHC*, JINST **3** (2008) S08004.

[37] P. Agostini et al., *The Large Hadron-Electron Collider at the HL-LHC*, J. Phys. G: Nucl. Part. Phys. **48** (2021) 110501.

[38] P. Azzi et al., *Report from Working Group 1: Standard Model Physics at the HL-LHC and HE-LHC*, CERN Yellow Rep. Monogr. **7** (2019) 1.

[39] S. Sekmen, *Beyond the Standard Model Physics at the High Luminosity LHC*, PoS **ICHEP2018** 283.

[40] M. Cacciari, G. P. Salam and G. Soyez, *The anti-k_t jet clustering algorithm*, JHEP **2008** (2008) 063.

[41] M. zur Nedden, *The LHC Run 2 ATLAS trigger system: design, performance and plans*, JINST **12** (2017) C03024.

Bibliography

[42] J. Alwall et al., *The automated computation of tree-level and next-to-leading order differential cross sections, and their matching to parton shower simulations*, JHEP **2014** (2014) 79.

[43] J. Alwall et al., *MadGraph 5: going beyond*, JHEP **2011** (2011) 128.

[44] P. Calafiura et al., *The Athena Control Framework in Production, New Developments and Lessons Learned*, CHEP (2005) 456.

[45] R. Brun and F. Rademakers, *ROOT: An object oriented data analysis framework*, Nucl. Instrum. Meth. A **389** (1997) 81.

[46] A. Buckley et al., *Rivet user manual*, Comput. Phys. Commun. **184** (2013) 2803.

[47] D. Perret-Gallix, *Computational particle physics for event generators and data analysis*, J. Phys. Conf. Ser. **454** (2013) 012051.

[48] S. Agostinelli et al., *Geant4-a simulation toolkit*, Nucl. Instrum. Methods Phys. Res. A **506** (2003) 250.

[49] V. Blobel, *Unfolding Methods in Particle Physics*, in *PHYSTAT 2011*. CERN, Geneva, 2011.

[50] V. Alekseev et al., *Reconstruction of particle's energy spectrum in experiment with Unfolding technique*, J. Phys. Conf. Ser **1390** (2019) 012071.

[51] The ATLAS collaboration, *Search for a heavy charged boson in events with a charged lepton and missing transverse momentum from pp collisions at $\sqrt{s}$= 13 TeV with the ATLAS detector*, Phys. Rev. D **100** (2019) 052013.

[52] The CMS collaboration, *Search for high-mass resonances in final states with a lepton and missing transverse momentum at $\sqrt{s}$ = 13 TeV*, JHEP **2018** (2018) 128.

[53] T. Sjöstrand et al., *An introduction to PYTHIA 8.2*, Comput. Phys. Commun. **191** (2015) 159.

[54] J. C. Pati and A. Salam, *Unified Lepton-Hadron Symmetry and a Gauge Theory of the Basic Interactions*, Phys. Rev. D **8** (1973) 1240.

[55] The CMS Collaboration, *Constraints on models of scalar and vector leptoquarks decaying to a quark and a neutrino at $\sqrt{s}$ = 13 TeV*, Phys. Rev. D **98** (2018) 032005.

[56] The ZEUS Collaboration, *A Search for resonance decays to lepton + jet at HERA and limits on leptoquarks*, Phys. Rev. D **68** (2003) 052004.

[57] F. Aaron et al., *Search for first generation leptoquarks in ep collisions at HERA*, Phys. Lett. B **704** (2011) 388.

[58] The CMS Collaboration, *Search for single production of scalar leptoquarks in proton-proton collisions at $\sqrt{s} = 8$* TeV, Phys. Rev. D **93** (2016) 032005.

[59] A. Djouadi, *The anatomy of electroweak symmetry breaking Tome II: The Higgs bosons in the Minimal Supersymmetric Model*, Phys. Rep. **459** (2008) 1.

[60] G. Branco et al., *Theory and phenomenology of two-Higgs-doublet models*, Phys. Rep. **516** (2012) 1.

[61] G. Senjanovic and R. N. Mohapatra, *Exact left-right symmetry and spontaneous violation of parity*, Phys. Rev. D **12** (1975) 1502.

[62] J. Cieza Montalvo et al., *Searching for doubly charged Higgs bosons at the LHC in a 3-3-1 model*, Nucl. Phys. B **756** (2006) 1.

[63] J. F. Gunion, R. Vega and J. Wudka, *Higgs triplets in the standard model*, Phys. Rev. D **42** (1990) 1673.

[64] H. Georgi and M. Machacek, *Doubly charged Higgs bosons*, Nucl. Phys. B **262** (1985) 463.

[65] O. Witzel, *Review on Composite Higgs Models*, PoS Proc. Sci **LATTICE2018** (2019) 006.

[66] *Theory and phenomenology of two-Higgs-doublet models*, Phys. Rep. **516** (2012) 1.

[67] V. Keus, S. F. King and S. Moretti, *Three-Higgs-doublet models: symmetries, potentials and Higgs boson masses*, JHEP **01** (2014) 052.

[68] M. Aaboud et al., *Search for charged Higgs bosons decaying via $H^{\pm} \to \tau^{\pm} \nu_{\tau}$ in the τ+jets and τ+lepton final states with 36 fb^{-1} of pp collision data recorded at $\sqrt{s} = 13$ TeV with the ATLAS experiment*, JHEP **2018** (2018) 139.

[69] LHC Higgs Cross Section Working Group Collaboration, *Handbook of LHC Higgs Cross Sections: 3. Higgs Properties: Report of the LHC Higgs Cross Section Working Group*. CERN Yellow Rep. Monogr. Jul, 2013.

[70] M. Pinamonti. Priv. comm. Jul., 2022.

Acknowledgements